

Article

VPSO-SVM-Based Open-Circuit Faults Diagnosis of Five-Phase Marine Current Generator Sets

Gang Yao ¹, Shuxiu Pang ², Tingting Ying ², Mohamed Benbouzid ^{2,3,*},
Mourad Ait-Ahmed ⁴ and Mohamed Fouad Benkhoris ⁴

¹ Sino-Dutch Mechatronics Engineering Department, Shanghai Maritime University, Shanghai 201306, China; gangyao@shmtu.edu.cn

² Electrical Engineering Department, Shanghai Maritime University, Shanghai 201306, China; shuxiupang@163.com (S.P.); diansanyt@126.com (T.Y.)

³ Institut de Recherche Dupuy de Lôme (UMR CNRS 6027 IRDL), University of Brest, 29238 Brest, France

⁴ IREENA, l'Université de Nantes/Polytech Nantes, 44602 Nantes, France; ait-ahmed-m@univ-nantes.fr (M.A.-A.); mohamed-fouad.benkhoris@univ-nantes.fr (M.F.B.)

* Correspondence: Mohamed.Benbouzid@univ-brest.fr

Received: 11 September 2020; Accepted: 10 November 2020; Published: 17 November 2020



Abstract: Generating electricity from enormous energy contained in oceans is an important means to develop and utilize marine sustainable energy. An offshore marine current generator set (MCGS) is a system that runs in seas to produce electricity from tremendous energy in tidal streams. MCGSs operate in oceanic environments with high humidity, saline-alkali water, and impacts of marine organisms and waves, and consequently malfunctions can happen along with the need for expensive inspection and maintenance. In order to achieve effective fault diagnosis of MCGSs in events of failure, this paper focuses on fault detection and diagnosis (FDD) of MCGSs based on five-phase permanent magnet synchronous generators (FP-PMSGs) with the third harmonic windings (THWs). Firstly, mathematical models were built for a hydraulic turbine and the FP-PMSG with THWs; then, a fault detection method based on empirical mode decomposition (EMD) and Hilbert transform (HT) was studied to detect different open-circuit faults (OCFs) of the generator; afterwards, a variable-parameter particle swarm optimization (VPSO) was designed to optimize the penalty and kernel function parameters of a support vector machine (SVM), which was named the VPSO-SVM method in this paper and used to perform fault diagnosis of the FP-PMSG. Finally, simulation blocks were built with MATLAB/Simulink to realize the mathematical models of the MCGS, and the proposed FDD method was coded with MATLAB. The effectiveness of the proposed VPSO-SVM method was validated by simulation results analysis and comparisons.

Keywords: fault detection and diagnosis; marine current generation; five-phase permanent magnet synchronous generator; third harmonic windings; empirical modal decomposition; Hilbert transform; particle swarm optimization; support vector machines

1. Introduction

1.1. Research Background and Motivations

With the global fossil energy shortage and ecological environment deterioration, development and utilization of renewable energy and reduction of pollutants emissions have become important directions of technology development world wide. Oceans cover 70% area of the Earth and hold tremendous energy in tidal streams that can be utilized for electricity generation [1]. Accordingly, marine current generation technology has attracted much attention in both research and industrial communities all over the world.

Marine current energy mainly refers to kinetic energy generated by the regular flow of seawater in undersea waterways and straits due to tidal movement [2,3]; and a marine current generator set (MCGS) could convert this kinetic energy into electrical energy. In this kind of generation system, due to attractive performance and good fault-tolerant control ability, multi-phase machines (MPMs) have been widely concerned in recent years and became a research hotspot [4–6]. Compared with traditional three-phase machines, MPMs have the following advantages:

- (1) When machine power and phase current are kept constant, increasing phase number of the machine can reduce phase voltage, resulting in large power output with lower voltage level. This can also avoid the current-sharing problem caused by power electronic devices in series and parallel connections [7].
- (2) An MPM can provide more control freedom than a three-phase machine; fault-tolerant operation could be achieved in an MPM if one or more phase is in fault conditions [8].
- (3) Compared to a traditional three-phase machine, the dynamic and static characteristics of an MPM are improved [9], making it more suitable for sustainable energy generation systems.

At present, one of the research focuses of MPMs lies in five-phase machines with third harmonic windings (THWs) in stators. Machines' output torque could be increased with the interactions of the third harmonic current and magnetic field [10]. Meanwhile, the injection of the third harmonic current into a five-phase machine can reduce magnetic saturation of the stator core and improve machine efficiency [11]. This kind of five-phase machine has important applications in marine energy generation and ship propulsion systems and, therefore, a five-phase permanent magnet synchronous generator (FP-PMSG) with THWs is adopted in this paper for MCGSs.

MCGSs operate under seawater with harsh marine environment, influences from ocean circumstances, such as moisture, saline corrosion, crash of marine organism etc., may lead to malfunctions of generators and converters of the MCGSs. Some common faults include short circuit faults (SCFs) and/or open-circuit faults (OCFs) in generators' winding and power conversion devices [12]. These failures will result in downtime and subsequent expensive operations for fault positioning and system maintenance. Accordingly, it is of great practical significance to research fault detection and diagnosis (FDD) technology for the development of marine current generation.

1.2. State of the Art of Marine Current Generation and Its Fault Detection and Diagnosis (FDD)

Marine current generation is a comparatively new technology that has developed rapidly in the last decade. The relevant research is mainly focused on the key technologies to enhance the energy capture capability of MCGSs [13]. To realize this purpose, many scholars are dedicated in the related topics, such as marine current generation system design, analysis and optimization [14–17], control methodology improvement [18–24], state monitoring and fault diagnosis [25–33], etc., for the development of MCGSs with high reliability and efficiency.

Among these research hotspots, state monitoring and fault diagnosis are important means to guarantee safety operations of MCGSs. Emerging FDD technologies of marine current turbines are mainly related to works that have been applied on wind turbines and the pulse-width modulation (PWM) inverter driving the multi-phase motor for high-performance motion control [14,34]. For example, in reference [25], a normalized mode-correlation principal component analysis method was proposed to deal with the fault detection difficulties caused by turbulence and wave of a MGCT. Reference [26] presented a new model-based online diagnostic indicator monitoring method for winding insulation of a marine tidal generator. The effects of temperature variation on the diagnostic model parameters were investigated. Experimental results showed that insulation capacitance increases as temperature increases. To deal with imbalance detection problem of marine pollutants attachment to the turbine blades, Reference [27] proposed an empirical mode decomposition and spectrum analysis-based blades imbalance fault detection method. Simulation and experimental results in different faulty conditions validated the effectiveness of the proposed method. Reference [28] designed a generator

stator current-based fault detection technique, which adopted a recursive maximum likelihood estimator to track the time-varying fault characteristic frequency, to deal with a wind turbines condition monitoring. Simulation results demonstrated the feasibility of the proposed approach of a wind turbine with electrical asymmetry and mechanical imbalance. In references [29,30], symmetrical components analysis based methods were proposed to extract five-phase machine fault features and diagnose OCFs and interturn faults respectively. Considering that many permanent magnet motors are driven by Pulse Width Modulation (PWM) inverters, reference [31,32] adopted high-frequency PWM ripple currents to detect interturn faults of a motor. Experiences in [31] showed that the ripple current ratios between two adjacent phases can detect turn fault with high signal-to-noise ratio. In [33], a Direct Current (DC) voltage injection method was proposed to monitor and detect stator interturn faults of five-phase motors. This method was operated within control loops to realize fault-tolerant control when faults were detected.

From the above literature review, it can be seen that although many interesting research findings had been achieved concerning MCGS FDD technologies, FDD research on FP-PMSG is still insufficient to meet the fast development requirements of MCGSs. The main insufficiencies include: (1) there is a lack of targeted research on fault detection, diagnosis and fault tolerance control of multi-phase current generators, especially on FP-PMSG with THWs. Many FDD methods applied on MCGs in the literature are from three-phase PMSG or multi-phase machine systems in different applications; (2) in practice, because MPMs are commonly used as motors in motion control applications with high safety requirements, their FDD methods are often connected with their feeding PWM converters. These approaches cannot be directly adopted in scenarios where MPMs are used as generators. Furthermore, in these applications, more research attention is paid to the study of fault tolerance control of MPMs to guarantee system safety than that to FDD, leading to insufficient research on FDD; and (3) concerning existing OCFs diagnosis research on five-phase machines, although different OCFs, such as OCFs of single phase, two adjacent phases, and two non-adjacent phases, could be differentiated, developing one FDD method to distinguish the above fault types, in order to identify the phase happening a single-phase OCF, and to differentiate OCF from sensor faults, still needs further research.

To deal with the above deficiencies, this paper adopts signal processing techniques instead of model-based approaches (for the purpose of reducing dependence on system models) to develop a FDD method for different OCFs of FP-PMSGs with THWs. To make the developed method non-intrusive to the generator and require fewer additional sensors, a method relying only on a five-phase terminal current of the FP-PMSG would be a good solution. But when there is a fault happening in the generator, its phase currents are non-stationary signals and stationary signal processing techniques are not suitable to apply [35]. For this reason, empirical mode decomposition, a non-stationary signal processing method, is adopted in this paper to realize non-stationary current decomposition. Then, with the obtained stationary signals, Hilbert transform (HT) is used to calculate fault indicator for fault detection and feature parameters for diagnosis. When realizing fault classification, it is necessary to consider that in reality MCGS fault samples are not easy to obtain and sample number could be small. The support vector machine (SVM), which is suitable for effective classification with small sample numbers, is used as a fault classifier. In order to improve the classification accuracy of SVM, a modified particle swarm optimization (PSO) method is further utilized to find the optimal parameters of SVM. Thereby, a hybrid approach, consisting of empirical mode decomposition (EMD) and HT techniques for fault detection, and PSO and SVM methods for fault diagnosis, is proposed in this paper to realize effective fault diagnosis of FP-PMSGs.

1.3. Organization of This Article

The rest of this paper is organized as follows: in Section 2, the basic structure and operation principle of a MCGS based on a FP-PMSG with THWs are analyzed, and mathematical models of its hydraulic turbine and the FP-PMSG are built. In Section 3, firstly a fault detection method based

on EMD and HT is studied, then a variable-parameter particle swarm optimization (VPSO)-SVM is proposed by combining the VPSO with SVM to realize fault diagnosis of the generator. In Section 4, an MCGS simulation platform is built according to the mathematical models presented in Section 2 with MATLAB/Simulink, and the proposed VPSO-SVM method is coded to diagnose different OCFs of the generator. Then, the results of simulation experiments carried out in normal working conditions and different OCFs in the FP-PMSG are presented. These simulation results are compared with those of single SVM and PSO-SVM without parameter tuning to verify the effectiveness of the proposed method. Finally, in Section 5, the work of this paper is summarized.

2. Mathematical Models of Five-Phase Permanent Magnet Synchronous Generator (FP-PMSG)-Based Marine Current Generator Set (MCGS)

2.1. MCGS Structure

The structure of the studied direct-drive MCGS is shown in Figure 1, which includes a hydraulic turbine, a non-salient and surface-mounted FP-PMSG, and a power converter [36].

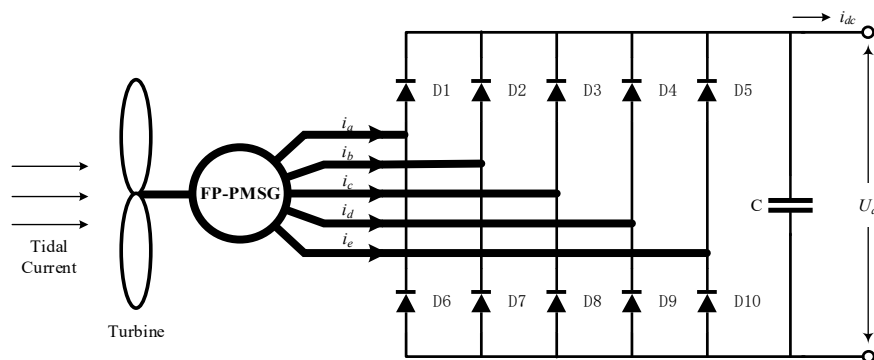


Figure 1. Structure of the studied marine current generator set (MCGS).

In Figure 1, the hydro turbine converts kinetic energy of sea current into mechanical energy and drives the generator to rotate; the non-salient FP-PMSG further converts the mechanical energy into electricity. Normally an Alternating Current (AC) to AC converter, including an uncontrollable five-phase rectifier, a Boost circuit and a three-phase power inverter, could be adopted to connect the generator to power grid. Consider the focus of this paper is the FDD technology of the FP-PMSG, only the diode-based uncontrollable five-phase rectifier is shown in the figure to connect the generator to the DC bus.

2.2. Hydro Turbine Model

2.2.1. Tidal Speed Model

The mathematical model of tidal speed is built by the addition of multiple cosine functions with an average current velocity and a white noise as follows [37]:

$$v(t) = v_0 + 0.025 \cos(0.314t) + 0.0275 \cos(0.618t) + 0.089 \cos(0.933t) + \dots + b(t) \quad (1)$$

where $v(t)$ presents the tidal speed, v_0 is its average value, and $b(t)$ is a Gaussian white noise signal.

2.2.2. Hydro Turbine Model

According to Baez's theory, the output mechanical power of the turbine is as follows [38].

$$P_m = \frac{1}{2} \rho \pi R^2 C_p(\lambda, \beta) v^3 \quad (2)$$

where P_m is the output mechanical power of the turbine, ρ represents sea water density, R is the turbine blades' radius, v is the velocity of the tidal current, C_p is hydro current energy utilization coefficient and is a function of pitch angle (noted as β) and tip speed ratio (noted as λ), where $\lambda = \omega_m R/v$, and ω_m is the angle velocity of the turbine.

Mechanical torque of the turbine, noted as T_m , then can be expressed with:

$$T_m = P_m / \omega_m \quad (3)$$

2.3. Model of Non-Salient FP-PMSG with Third Harmonic Windings (THWs)

The dynamic model in rotating reference frame of the non-salient and surface-mounted FP-PMSG with THWs shown in Figure 1 can be obtained by applying coordinate transformation to the generator's mathematical model in stationary reference frame. The transformation matrix T is:

$$T = \frac{2}{5} \begin{bmatrix} \cos \theta & \cos(\theta - \frac{2}{5}\pi) & \cos(\theta - \frac{4}{5}\pi) & \cos(\theta - \frac{6}{5}\pi) & \cos(\theta - \frac{8}{5}\pi) \\ -\sin \theta & -\sin(\theta - \frac{2}{5}\pi) & -\sin(\theta - \frac{4}{5}\pi) & -\sin(\theta - \frac{6}{5}\pi) & -\sin(\theta - \frac{8}{5}\pi) \\ \cos 3\theta & \cos 3(\theta - \frac{2}{5}\pi) & \cos 3(\theta - \frac{4}{5}\pi) & \cos 3(\theta - \frac{6}{5}\pi) & \cos 3(\theta - \frac{8}{5}\pi) \\ -\sin 3\theta & -\sin 3(\theta - \frac{2}{5}\pi) & -\sin 3(\theta - \frac{4}{5}\pi) & -\sin 3(\theta - \frac{6}{5}\pi) & -\sin 3(\theta - \frac{8}{5}\pi) \\ \frac{1}{2} & \frac{1}{2} & \frac{1}{2} & \frac{1}{2} & \frac{1}{2} \end{bmatrix} \quad (4)$$

where θ is electric angle of rotor.

The stator voltage equations of the generator in dq frame are written as [39]:

$$\begin{cases} u_{d1} = Ri_{d1} + L_{d1} \frac{di_{d1}}{dt} - \omega_e L_{q1} i_{q1} \\ u_{q1} = Ri_{q1} + L_{q1} \frac{di_{q1}}{dt} + \omega_e (L_{d1} i_{d1} + \psi_{m1}) \\ u_{d3} = Ri_{d3} + L_{d3} \frac{di_{d3}}{dt} - 3\omega_e L_{q3} i_{q3} \\ u_{q3} = Ri_{q3} + L_{q3} \frac{di_{q3}}{dt} + 3\omega_e (L_{d3} i_{d3} + \psi_{m3}) \end{cases} \quad (5)$$

where u_{d1} , u_{q1} , u_{d3} and u_{q3} are stator voltage components in direct and quadrature axes, i_{d1} , i_{q1} , i_{d3} and i_{q3} are stator current components in direct and quadrature axes, L_{d1} , L_{q1} , L_{d3} and L_{q3} are inductance in direct and quadrature axes, R is stator resistance, ω_e is electric angular speed of the rotor, ψ_{m1} and ψ_{m3} are fundamental and the third harmonics flux-linkage of the permanent magnet.

The electromagnet torque of the FP-PMSG with THWs is [39]:

$$T_e = \frac{5}{2} p \left[(L_{d1} i_{d1} + \psi_{m1}) i_{q1} - L_{q1} i_{q1} i_{d1} + 3(L_{d3} i_{d3} + \psi_{m3}) i_{q3} - 3L_{q3} i_{q3} i_{d3} \right] \quad (6)$$

where T_e is electromagnetic torque of the FP-PMSG, and p is the number of pole pairs.

For a non-salient and surface-mounted FP-PMSG, $L_{d1} = L_{q1}$ and $L_{d3} = L_{q3}$, thus Equation (6) could be simplified as follows.

$$T_e = \frac{5}{2} p \left[\psi_{m1} i_{q1} + 3\psi_{m3} i_{q3} \right] \quad (7)$$

Consider that a direct-drive MCGS without gearboxes is adopted in this paper, the motion equation of the generator is as follows when the damping of rotation shaft is not considered:

$$T_m - T_e = J \frac{d\omega_m}{dt} \quad (8)$$

where J is rotor rotation inertia.

3. Faults Detection and Diagnosis of FP-PMSG

As discussed in Section 1.2, phase currents of a generator are normally nonstationary signals when there is a fault happening [35]. To realize fault detection and feature extraction of diagnosis,

EMD, a technique that can adaptively decompose a nonstationary signal into a series of intrinsic mode functions (IMFs) (representing characteristics of the nonstationary signal) and a residue [40], is adopted in this paper to decompose direct-axis component of generator's output currents; then, analytic signals are calculated by applying Hilbert transform to the IMFs and residue; afterwards, the instantaneous amplitude, phase and frequency of the complex analytic signals could be obtained to determine an indicator for fault detection and feature parameters for fault diagnosis. With these features, the VPSO-SVM is designed in this section to identify the faults.

3.1. Empirical Mode Decomposition (EMD)-Hilbert Based Fault Detection and Fault Feature Parameters Extraction

According to the principle of EMD, a non-stationary signal, noted as $x(t)$, including fault characteristics can be represented by a number of IMFs with a residual as follows [40]:

$$x(t) = \sum_{i=1}^k c_i(t) + r(t) \quad (9)$$

where $c_i(t)$ ($i = 1, \dots, n$) denotes the i th IMF, and $r(t)$ is the residual.

Apply Hilbert transform to the IMFs with the following equation [41]:

$$H[c_i(t)] = \frac{1}{\pi} \int_{-\infty}^{+\infty} \frac{c_i(\tau)}{t - \tau} d\tau = c_i(t) * \frac{1}{\pi\tau} \quad (10)$$

where τ is a time variable.

The instantaneous amplitude, noted as $A_i(t)$, phase, noted as $\phi_i(t)$, and frequency, noted as $\omega_i(t)$ of the analytic signal could be obtained with:

$$A_i(t) = \sqrt{c_i^2(t) + H^2[c_i(t)]} \quad (11)$$

$$\phi_i(t) = \text{tg}^{-1} \frac{H[c_i(t)]}{c_i(t)} \quad (12)$$

$$\omega_i(t) = \frac{d\phi_i(t)}{dt} \quad (13)$$

With Equation (11), the instantaneous amplitudes of the IMFs are calculated and selected as an OCF indicator of the FP-PMSG in this paper. In order to realize fault identification when OCFs occur, the instantaneous amplitude, phase and frequency are grouped together as fault features for further fault diagnosis.

3.2. Support Vector Machine (SVM)-Based Fault Classification

Fault classification is based on pattern recognition theory and can be carried out by designing a fault classifier [42]. SVM is a pattern classification method as well as a supervisory learning algorithm, which could be trained by historical sample data in both normal and faulty conditions and then used for faults identification.

The idea of SVM is to map its input vector to a high-dimensional feature space through a non-linear mapping function, and in this space, an optimal hyperplane based on a non-linear kernel function is constructed for classification. The optimal classification hyperplane can be written as follows [43]:

$$f(x) = \text{sgn} \left[\sum_{i=0}^n \alpha_i y_i K(x_i, x_j) + b \right] \quad (14)$$

This hyperplane equation can be used to minimize the following target function $\varphi(\omega, \xi)$:

$$\varphi(\omega, \xi) = \frac{1}{2} \|\omega^2\| + C \sum_{i=1}^n \xi_i \quad (15)$$

where $x_i, x_j \in R^n$ are two input data, $y_i \in \{+1, -1\}$ is the binary output, α_i is the Lagrange multiplier, b is an offset value, ω is normal direction vector of the optimal hyperplane, $\xi_i \geq 0$ is a slack variable; $C > 0$, is a penalty factor to avoid giving up important data; $K(x_i, x_j)$ is a kernel function, and radial basis function (RBF) is adopted in this paper as follows [44]:

$$K(x_i, x_j) = \exp(-g \sum_{i=0}^n (x_i - x_j)^2) \quad (16)$$

where g is width parameter of the radial basis kernel function.

The penalty factor C and the parameter g are two important parameters of the RBF-based SVM. The parameter C affects classification accuracy of the SVM and controls penalty degree of faultily classified samples. The kernel function parameter g reflects a mapping from input space to feature space, its value affects the feature space complexity of sample data as well as classifier's empirical error.

Accordingly, the values of penalty C and kernel parameter g determine data classification effect in characteristic spaces. In order to obtain a classifier with superior performance, it is important to optimize the values of C and g [45]. In this paper, the PSO method with a swarm average fitness-based parameter variation mechanism is proposed to optimize these two parameters.

3.3. Variable-Parameter Particle Swarm Optimization (VPSO) for SVM Parameters Optimization

PSO is a heuristic iteration algorithm inspired by bird flocks and has been widely adopted for optimal solution searching in different domains [46]. Suppose in an n -dimensional space, a swarm has a total of m particles to form a population x represented by $x = (x_1, x_2, \dots, x_m)^T$, location and velocity of the i th particle in the swarm are $x_i = (x_{i1}, x_{i2}, \dots, x_{in})^T$ and $v_i = (v_{i1}, v_{i2}, \dots, v_{in})^T$, respectively. The particles evaluate their fitness according to their position, and update individual's best value $p_i = (p_{i1}, p_{i2}, \dots, p_{in})^T$ and global best value $p_g = (p_{g1}, p_{g2}, \dots, p_{gn})^T$. The velocity and location of the i th particle then are updated with the following iterative equations [47].

$$v_i^{k+1} = \omega v_i^k + c_1 r_1 (p_i^k - x_i^k) + c_2 r_2 (p_g^k - x_i^k) \quad (17)$$

$$x_i^{k+1} = x_i^k + v_i^{k+1} \quad (18)$$

where c_1 and c_2 are cognitive learning rate and social learning rate respectively; ω is inertia weight; r_1 and r_2 are two random parameters within $[0, 1]$; The superscript k represents iteration steps.

The particle speed updating expression shown in Equation (17) consists of three parts: ωv_i^k indicates a particle can remember its speed of last iteration; $c_1 r_1 (p_i^k - x_i^k)$ represents local search capability of the particle and its ability to move towards the best location ever experienced; $c_2 r_2 (p_g^k - x_i^k)$ represents global search ability of the particle and its ability to move towards the global best location.

Among the parameters of the above PSO algorithm, c_1 , c_2 and ω are essential ones to determine PSO convergence speed. Tuning these parameters during iteration process instead of setting them constants could avoid PSO to trap into local optimization and converge prematurely. Accordingly, a swarm average fitness-based parameter variation mechanism is designed in this paper to decrease PSO convergent time.

According to the above analysis, the cognitive learning rate c_1 and social learning rate c_2 represent the particle's ability to search the individual and global best positions, and the inertial weight ω represents a particle's ability to keep its previous speed. To enhance local searching capability of the particles and to improve algorithm's convergency, in the VPSO method proposed in of this paper, if the

average fitness of the swarm increases along with iterations, which means the searching trajectory in the solution space is moving in the right direction, the values of c_1 and c_2 are increased to reinforce the particles' tracking ability of local and global best locations; at the same time, the value of ω is decreased to weaken the memory of its last location. By contrast, if the swarm's average fitness decreases, which indicates the searching may be not heading in the right direction, the value of ω is increased to strengthen its memory; meanwhile, the values of c_1 and c_2 are decreased. In case the average fitness values keep constant in the last several iteration steps when the desired value has not been reached, which probably indicates a local optimization, small random values are added to c_1 , c_2 and ω as perturbations to help the algorithm to jump out the local minimum. This parameter tuning method could be expressed in Table 1.

Table 1. Parameter tuning method of variable-parameter particle swarm optimization (VPSO).

Parameter Tuning Method	Conditions	Comments
$c_1^{k+1} = c_1^k \times \alpha_{c1}$ $c_2^{k+1} = c_2^k \times \alpha_{c2}$ $\omega^{k+1} = \omega^{k+1} \times \alpha_{\omega}$	$fit_{ave}^{k+1} > fit_{ave}^k$	where α_{c1} , α_{c2} and α_{ω} are parameter adjustment coefficients, which satisfy $\alpha_{c1} > 1$, $\alpha_{c2} > 1$ and $0 < \alpha_{\omega} < 1$.
$c_1^{k+1} = c_1^k + \alpha_{rand}$ $c_2^{k+1} = c_2^k + \alpha_{rand}$ $\omega^{k+1} = \omega^{k+1} + \alpha_{rand}$	$fit_{ave}^k \text{ keeps same}$	fit_{ave} is average fitness, its superscript k indicates iteration steps. α_{rand} is a random value between 0 and 1.
$c_1^{k+1} = c_1^k / \alpha_{c1}$ $c_2^{k+1} = c_2^k / \alpha_{c2}$ $\omega^{k+1} = \omega^{k+1} / \alpha_{\omega}$	$fit_{ave}^{k+1} < fit_{ave}^k$	

3.4. Working Flow of VPSO-SVM-Based Fault Diagnosis

Apply the variable-parameter PSO method described in Section 3.3 to optimize the penalty C and kernel parameter g of the SVM explained in Section 3.2, the VPSO-SVM algorithm is obtained. The working flow to train a VPSO-SVM fault classifier is as follows:

Step 1. Collect sample data in different fault modes and extract features

Collect output currents of the FP-PMMSG of a MCGS with different OCFs, apply frame transformation (Equation (4)) to obtain direct-axis components of the currents.

Step 2. Feature extraction

Apply EMD to the direct-axis current, then apply Hilbert transform to the IMFs and residue obtained to get their complex analytic signals; calculate instantaneous amplitude, phase and frequency of the analytic signals with Equations (11)–(13) as features of different OCFs. Assign a fault label to each feature according to the OCF it presents.

Step 3. VPSO parameters initialization

Initialize particles with randomly two-dimensional values of (C_i, g_i) to form a swarm (where i stands for the i th particle) and initialize velocities randomly. Define PSO parameters such as maximum iteration steps, population size, boundaries of velocities, etc.

Step 4. Define a fitness function and calculate initial fitness values

Define classification accuracy of SVM with cross-validation as a fitness function of the VPSO. Calculate fitness values of initial particles with the extracted features and their corresponding labels. Record individual and global best positions of initial swarm.

Step 5. Iterate and search particles' best location with variable PSO parameters

PSO iterates to search best location (two-dimensional values of (C_i, g_i)) with the minimum fitness values. During the iteration process, the parameters of PSO are tuned according to the method shown in Table 1.

Step 6. Obtain best location of PSO and pass the best values to SVM

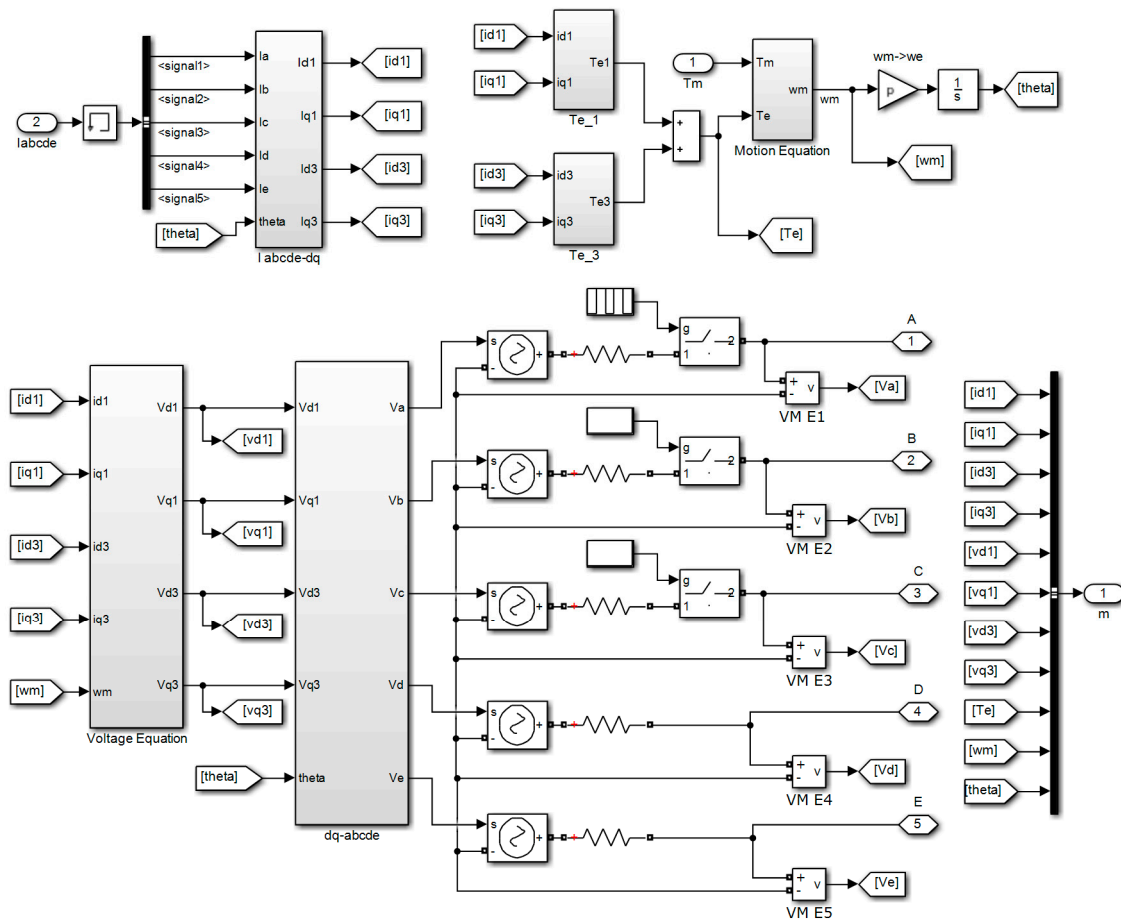
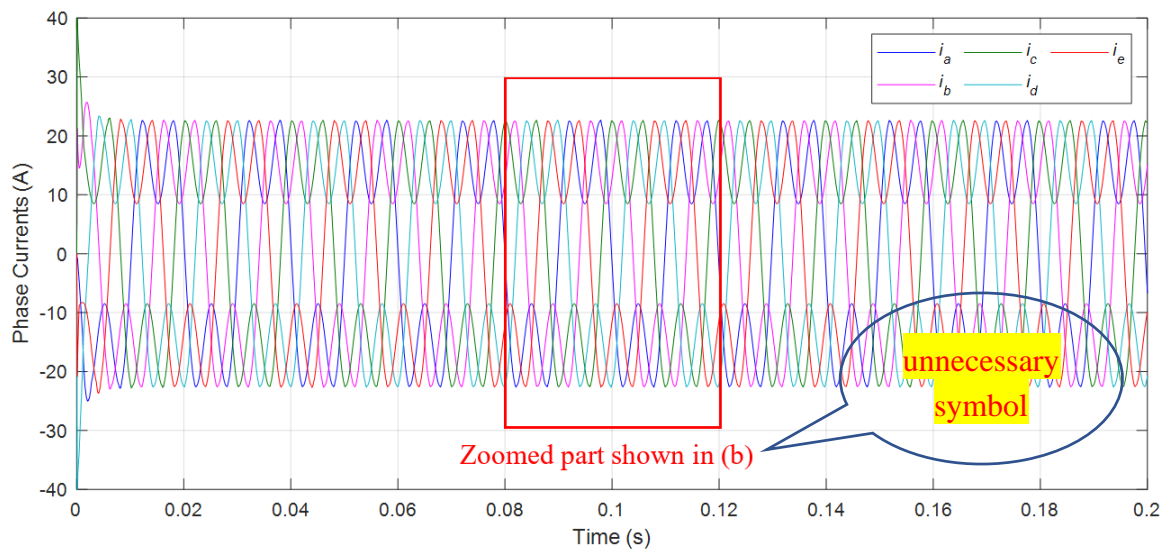


Figure 3. Simulation blocks of the FP-PMSG with third harmonic windings (THWs).

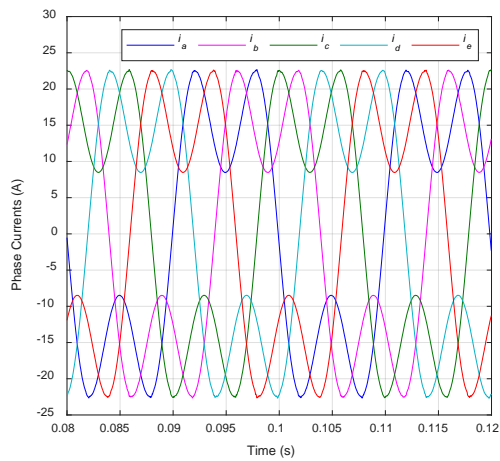
4.1. MCGS Simulation with No Faults

To verify the correctness of the FP-PMSG model, the simulation platform shown in Figure 2 was tested by running it for 0.2 s without faults. The average value of tidal speed v_0 in Equation (1) was set to 3.6 m/s. The terminal currents of the FP-PMSG, the zoomed part of the currents between 0.08 s and 0.12 s, and the fast Fourier transformation (FFT) of the terminal current of phase a are shown in Figure 4. The DC bus voltage is shown in Figure 5.

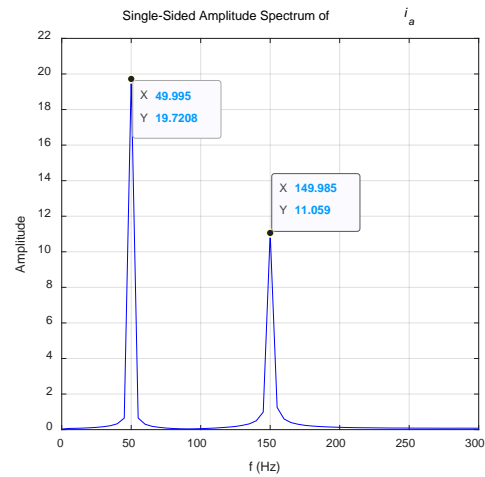
From Figure 4a,b, it could be seen that the output currents of the five-phase generator are not sinusoidal waves because of the third harmonic currents. After FFT to phase current i_a , as can be seen in Figure 4c, the main components of i_a are 49.995 Hz current and its threefold-frequency harmonic current of 149.985 Hz. From Figure 5, it could be seen that when there is no faults happened in the generator, the DC bus voltage is stable around 440 V with 10 kΩ resistive load connected.



(a)



(b)



(c)

Figure 4. Terminal currents of the FP-PMSG with THWs without faults and Fast Fourier transformation of phase *a* current. (a) Terminal currents of the FP-PMSG with THWs in normal condition with $v_0 = 3.6$ m/s. (b) Zoomed terminal currents of FP-PMSG between 0.07 s and 0.12 s. (c) Fast Fourier transformation of the terminal current of phase *a*.

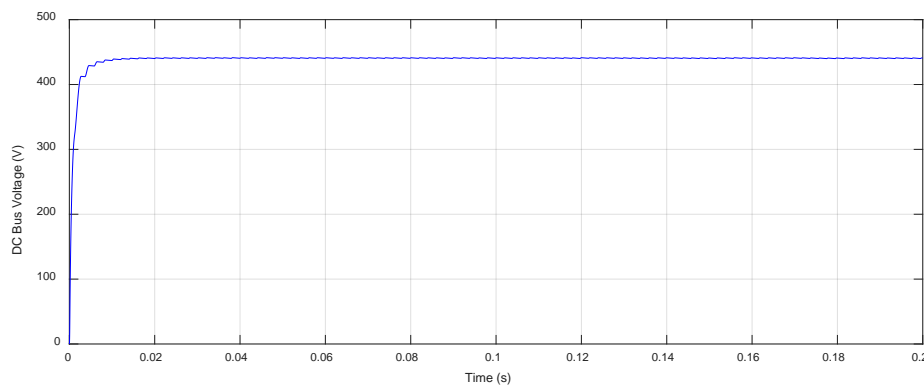


Figure 5. DC bus voltage during the 0.2 s simulation without faults.

4.2. FP-PMSG Open-Circuit Faults (OCFs) Detection Simulations

Open circuits and short circuits are common faults happening in FP-PMSGs. If a short circuit failure happens, by isolating the fault, the failure can be converted to an OCF. Accordingly, the detection and diagnosis of OCFs became the main concerns of this paper.

The OCFs of the FP-PMSG considered in the paper include the following three types:

- (1) single-phase OCFs, for example OCFs in phase *a*.
- (2) OCFs in two adjacent phases, for example OCFs concurrently in phase *a* and *b*.
- (3) OCFs in two non-adjacent phases, for example OCFs concurrently in phase *a* and *c*.

These faults were realized with the *Ideal Switch* blocks connected in the generator phases shown in Figure 3.

A simulation was carried out on the platform for 0.7 s with the following faults occurrence sequence:

- (1) during the first 0.1 s of the simulation, the MCGS was running normally;
- (2) at 0.1 s, an OCF happened in single-phase *a* and was revoked at 0.2 s;
- (3) the MCGS was running in normal condition from 0.2 s to 0.3 s;
- (4) at 0.3 s, OCFs simultaneously happened in two adjacent phases *a* and *b*, and the faults were both removed at 0.4 s;
- (5) the MCGS was running in normal condition from 0.4 s to 0.5 s;
- (6) at 0.5 s, OCFs happened again concurrently in two non-adjacent phases *a* and *c*, and the faults were both revoked at 0.6 s;
- (7) from 0.6 s to 0.7 s, the MCGS operated with no faults.

After running the simulation, the phase currents of the generator are plotted in Figure 6. Converted the five-phase currents of the generator from *abcde* stationary frame to $d_1q_1-d_3q_3_0$ frame with the transformation matrix shown in Equation (4) to obtain direct-axis component of the fundamental current (noted as i_{d1}), then applied EMD to i_{d1} to obtain its IMFs. The direct-axis current is shown in Figure 7a and its five IMFs are shown in Figure 7b. We applied the Hilbert transform to the five IMFs and further calculated the instantaneous amplitude, phase and frequency of the obtained complex analytic signals with Equations (11)–(13), and the calculation results are shown in Figure 8.

From Figure 6, it can be observed that:

- (1) during the four intervals when there were no faults (namely intervals of 0–0.1 s, 0.2–0.3 s, 0.4–0.5 s and 0.5–0.6 s), the currents of five phases had same amplitudes with peak values of 22.67 A.
- (2) From 0.1 s to 0.2 s, when an OCF happened in single-phase *a*, its current became zero, meanwhile, the currents of its two adjacent phases, *b* and *e*, increased with peak values of 27.55 A and 27.83 A, respectively. The currents of phases *c* and *d* had no obvious increments.
- (3) From 0.3 s to 0.4 s, when OCFs happened in two adjacent phases *a* and *b*, their currents both became zero, at the same time, the currents of its two adjacent phases, *c* and *e*, increased and reached peak values of 27.88 A and 27.78 A, respectively. The current peak value of phase *d* decreased to 19.74 A.
- (4) From 0.5 s to 0.6 s, when OCFs happened in two non-adjacent phases *a* and *c*, their currents both became zero, the current peak value of phase *b* decreased to 23.63 A and phases *d* and *e* increased to 25.88 A and 26.01 A, respectively.

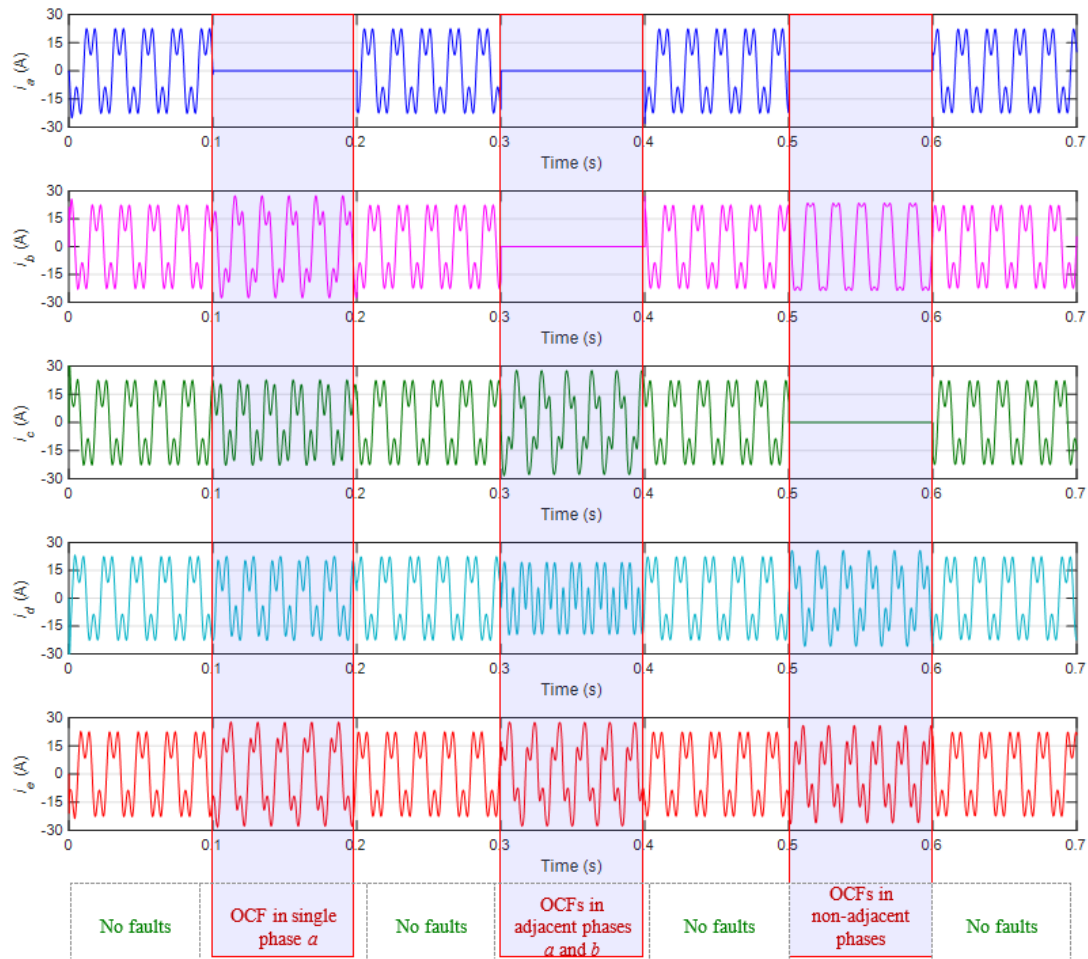
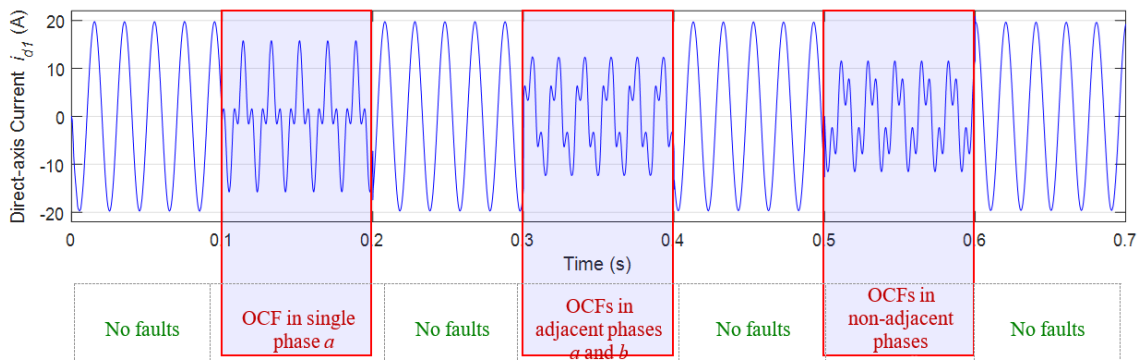


Figure 6. Phase currents of the FP-PMSG with three different open-circuit faults (OCFs) in the generator.

From Figure 7a, it could be seen that after reference frame transformation, the direct-axis current i_{d1} could present distinguishing patterns during the periods with different OCFs. After EMD was applied to i_{d1} , the first three IMFs exhibited sudden changes at those instances when OCFs arose and were revoked, and these can be seen in Figure 7b. Although the faults also had some influences on the IMF4 and IMF5 in Figure 7b, it was not easy to detect the faults from their occurring.



(a)

Figure 7. Cont.

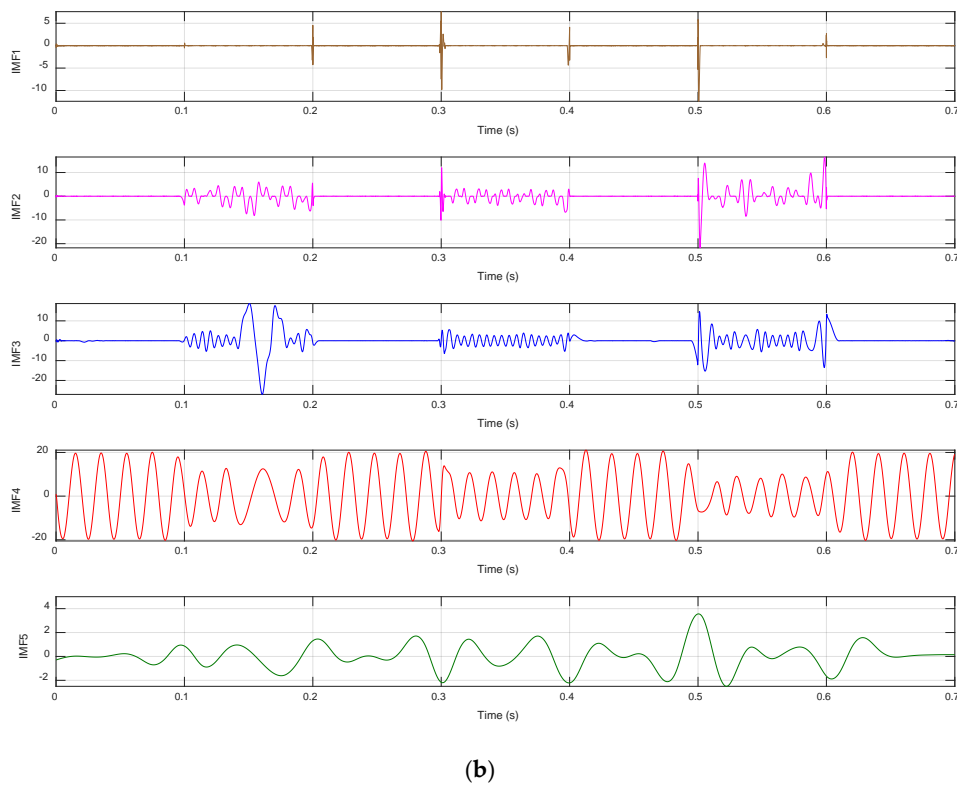


Figure 7. Direct-axis current and its five intrinsic mode functions (IMFs). (a) Direct-axis component of five-phase fundamental currents with three different OCFs in the generator. (b) Five IMFs of the direct-axis current.

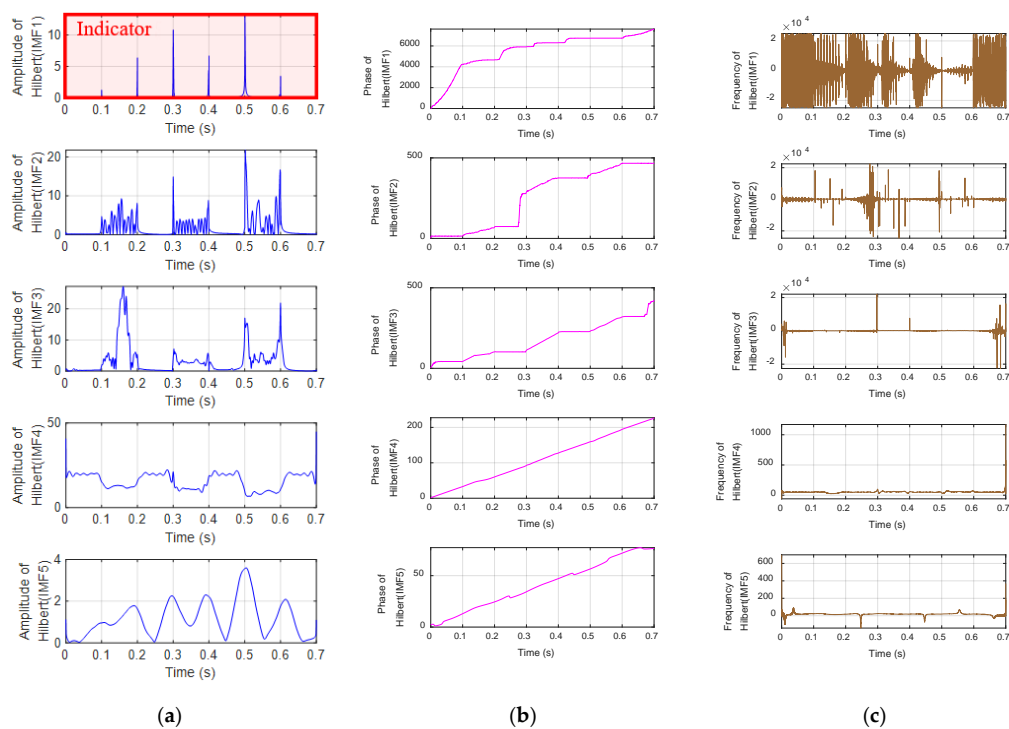


Figure 8. Instantaneous amplitude, phase and frequency of the analytic signals after Hilbert transform applied to the five IMFs. (a) Instantaneous amplitude of the five IMFs after Hilbert transform. (b) Instantaneous phase of the five IMFs after Hilbert transform. (c) Instantaneous frequency of the five IMFs after Hilbert transform.

These observations could be further verified in Figure 8. In Figure 8a, obvious changes or fluctuations during the OCF periods could be seen in the instantaneous amplitude curves of the first three IMFs after Hilbert transform, these abnormal changes are very helpful for fault detection. Although the OCFs also affected the remaining two signals in Figure 8a, the plots of phase shown in Figure 8b and the plots of frequency shown in Figure 8c, it was not easy to identify the times the OCFs occurred from them. Accordingly, the instantaneous amplitude of the first IMF after Hilbert transform is selected in this paper as an OCF indicator.

Another simulation was carried out for OCFs detection with the above fault indicator. Supposed the simulation lasted 0.7 s, from 0.35 to 0.45 s and from 0.55 to 0.6 s, OCFs happened in phase *a* two times; from 0.2 to 0.55 s, an OCF happened in phase *b*; from 0.05 to 0.15 s and from 0.5 to 0.65 s, OCFs happened in phase *c* also two times. The output currents of these three faulty phases and the fault indicator are shown in Figure 9.

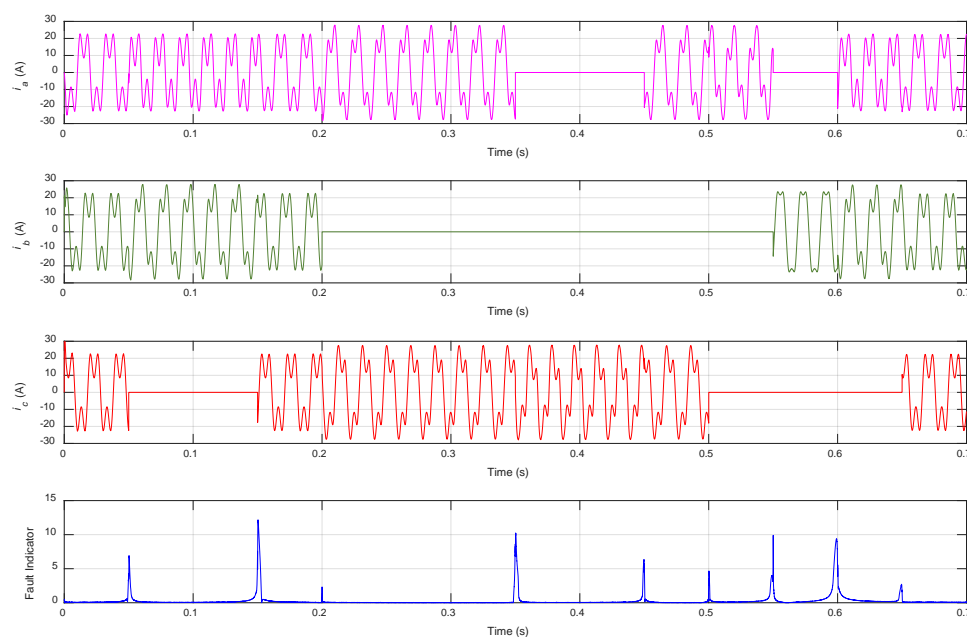


Figure 9. Output currents of three faulty phases with fault indicator.

From Figure 9, it can be seen that the OCF indicator showed a spike at each instance to point out the happening or ending time of the OCFs in the generator. For a real MCGS, an OCF in the generator will not be removed automatically, so the OCF indicator only indicates the time of fault occurrence.

An interesting issue that deserves further discussion is that this fault indicator not only can indicate the occurrence of faults, but also can help to distinguish whether the reason leading to zero output current of a phase is because of faults in generator or in current sensors. Imagine that when the generator is running normally without faults, an OCF happens in a current sensor installed on the terminal of the machine. The measured phase current by this sensor becomes zero, which is the same phenomenon as an OCF occurring in the generator winding. This is why it is not so reliable to identify OCFs directly using terminal currents.

The proposed indicator of this paper can avoid the above misdiagnosis. No matter it is because the OCFs in generator phases or in current sensors, the indicator will both generate a spike to indicate the faults, and the spike amplitude can distinguish the two different reasons.

To verify this important feature of the proposed indicator, simulations were carried out for comparisons. The simulations all lasted 0.2 s, and the three different OCFs happened at 0.1 s on the generator windings or terminal sensors. The plots of the indicator are shown in Figure 10.

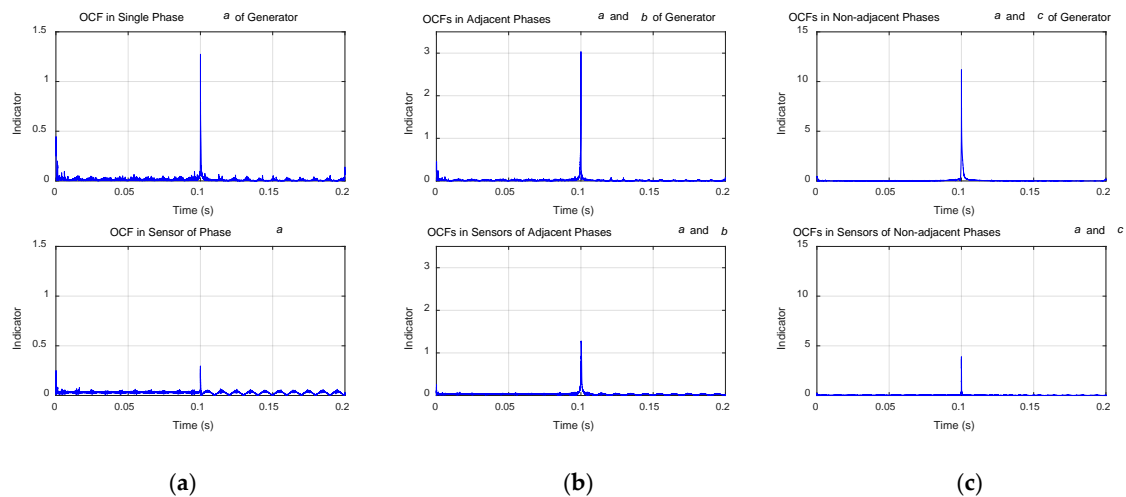


Figure 10. Indicate spike amplitudes distinguishing two different reasons leading to zero terminal phase current. (a) An OCF occurs in a generator’s single phase a , or its current sensor; (b) OCFs occur in generator’s two adjacent phases a and b , or their current sensors; (c) OCFs occur in generator’s two non-adjacent phases a and c , or their current sensors.

From the two subplots of Figure 10a, it can be seen that when an OCF happens in a single phase of the FP-PMSG, the spike of the indicator has much higher amplitude than the spike value caused by faulty sensor of a health generator. The same results could also be found in Figure 10b,c. If the FP-PMSG with THWs really has OCFs in its windings, the proposed indicator generates a spike with higher amplitude than that of a health machine with faulty current sensors.

4.3. Three Different FP-PMSG OCFs Diagnosis Simulations and Results Comparison

In order to distinguish the three different OCFs detected by the indicator, fault diagnosis needs to be further carried out according to the features of the fault.

As discussed in Section 3, the instantaneous amplitude, phase and frequency of the complex analytic signals obtained by applying Hilbert transform on i_{d1} ’s five IMFs and residue are adopted in this paper as fault features. Accordingly, for each sampled i_{d1} , a 1-by-18 vector is calculated as the fault feature.

Follow up the first simulation carried out in Section 4.2 for fault diagnosis, the proposed VPSO-SVM is applied in this section to identify the three different OCFs. The phase currents, their direct-axis component i_{d1} , the EMD results of i_{d1} , and their Hilbert transform results were already shown in the last section from Figure 6 to Figure 8.

Totally 600 samples were extracted from the three OCFs during the simulation: 200 from 0.1 to 0.2 s when there was an OCF in phase a , 200 from 0.3 to 0.4 s when two OCFs simultaneously happened in two adjacent phases a and b , and 200 from 0.5 to 0.6 s when two OCFs concurrently happened in two non-adjacent phases a and c . All samples were evenly distributed over time. Here, a 600-by-18 feature matrix was obtained. Classification labels were assigned for the three different OCFs as follows:

- Label “1” is for OCF in the single-phase a ,
- Label “2” is for OCFs in both phase a and b ,
- Label “3” is for OCFs in phase a and c .

The collected samples and their labels are shown in Figure 11.

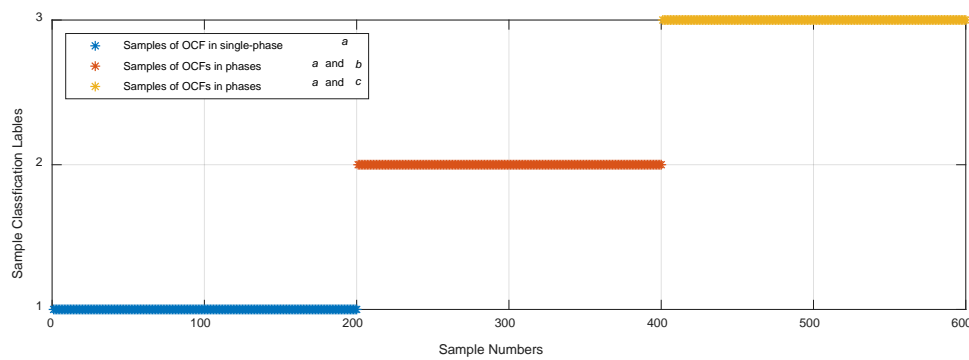


Figure 11. The 600 samples with their corresponding labels.

Among the 200 samples of each faults, 100 were taken to train an SVM and the remainder were used to test the trained SVM. Thus, the training and testing sets both had 300 samples for the three different faults. These samples were loaded to the proposed VPSO-SVM method coded in MATLAB. To compare the effectiveness of the proposed method, the fault features matrix was also applied to an SVM with constant C and g , and a PSO-SVM method with Constant parameters in PSO (hereby named CPSO-SVM). These three contrastive methods had same settings in common parameters, which are summarized in Table 3.

Table 3. Parameter configuration for the three contrastive methods.

	Parameters	Values
PSO	Size of swarm	20
	Maximum number of iterations	200
	Initial value of c_1 (Fixed in CPSO-SVM)	1.5
	Initial value of c_2 (Fixed in CPSO-SVM)	1.5
	Initial value of ω (Fixed in CPSO-SVM)	1
	Range of penalty factor C	[0.01 10]
	Range of kernel function parameter g	[0.01 10]
	Adjustment coefficients [α_{c1} α_{c2} α_{ω}]	[1.15 1.15 0.98]
SVM	penalty factor C (for SVM with fixed parameters)	2
	kernel parameter g (for SVM with fixed parameters)	1
	Cross validation set number	5
	Number of training samples	100
	Number of testing samples	100

To remove the disturbances from randomly generated values in PSO on the classification results, the initial values of particles were fixed with a same set of random values created by the *rand* function of MATLAB.

The fault classification results on the testing set by SVM with fixed parameters C and g is shown in Figure 12. The PSO iteration process and fault classification results on the testing set by CPSO-SVM are shown in Figure 13. The PSO parameter variation plots along with iterations, PSO iteration process, and fault classification results on the testing set by the proposed VPSO-SVM are shown in Figure 14. The simulation results' statistical data of the three comparative methods are summarized in Table 4.

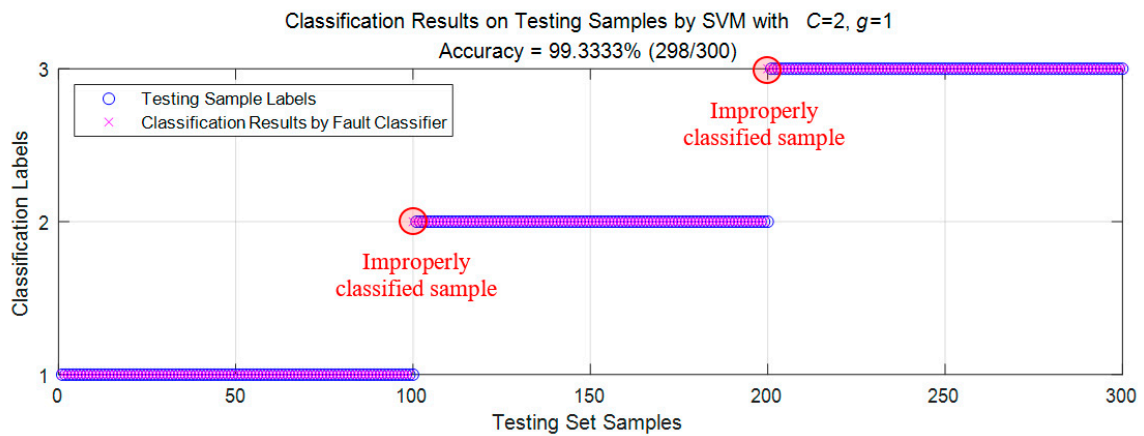
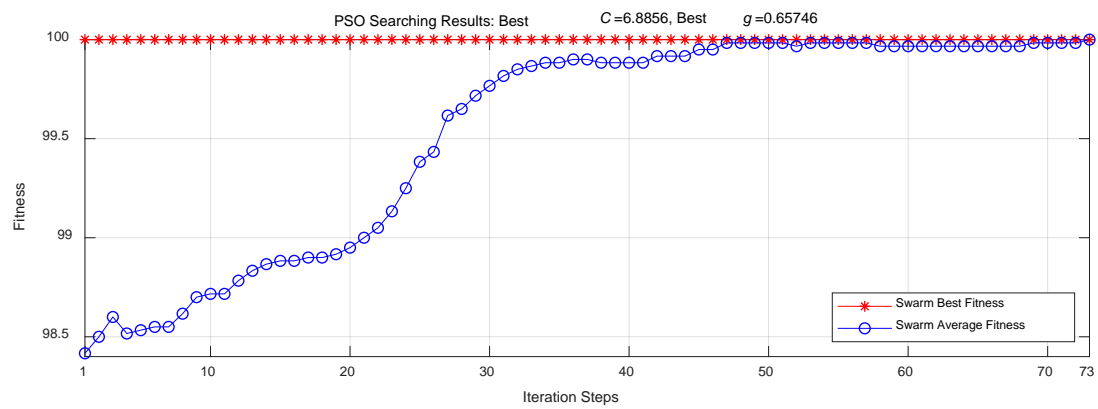
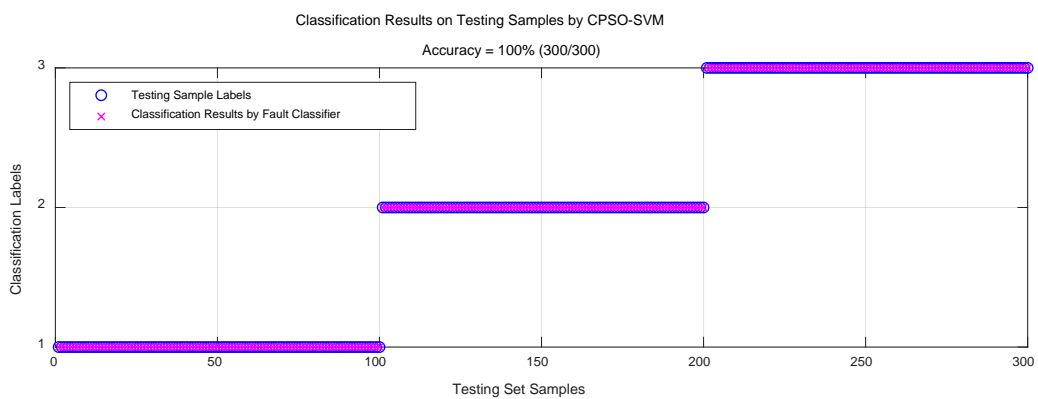


Figure 12. Fault classification results on testing set by support vector machine (SVM) with assigned parameters $C = 2$ and $g = 1$ (classification accuracy = 99.33%).



(a)



(b)

Figure 13. Fault classification results on testing set by CPSO-SVM with SVM parameters $C = 6.8856$ and $g = 0.65746$ optimized by CPSO. (a) Swarm average fitness evolving process along with iterations (73 iteration steps to converge with constant $c_1 = c_2 = 1.5$ and $\omega = 1$ in PSO). (b) Fault classification results of CPSO-SVM (classification accuracy = 100%).

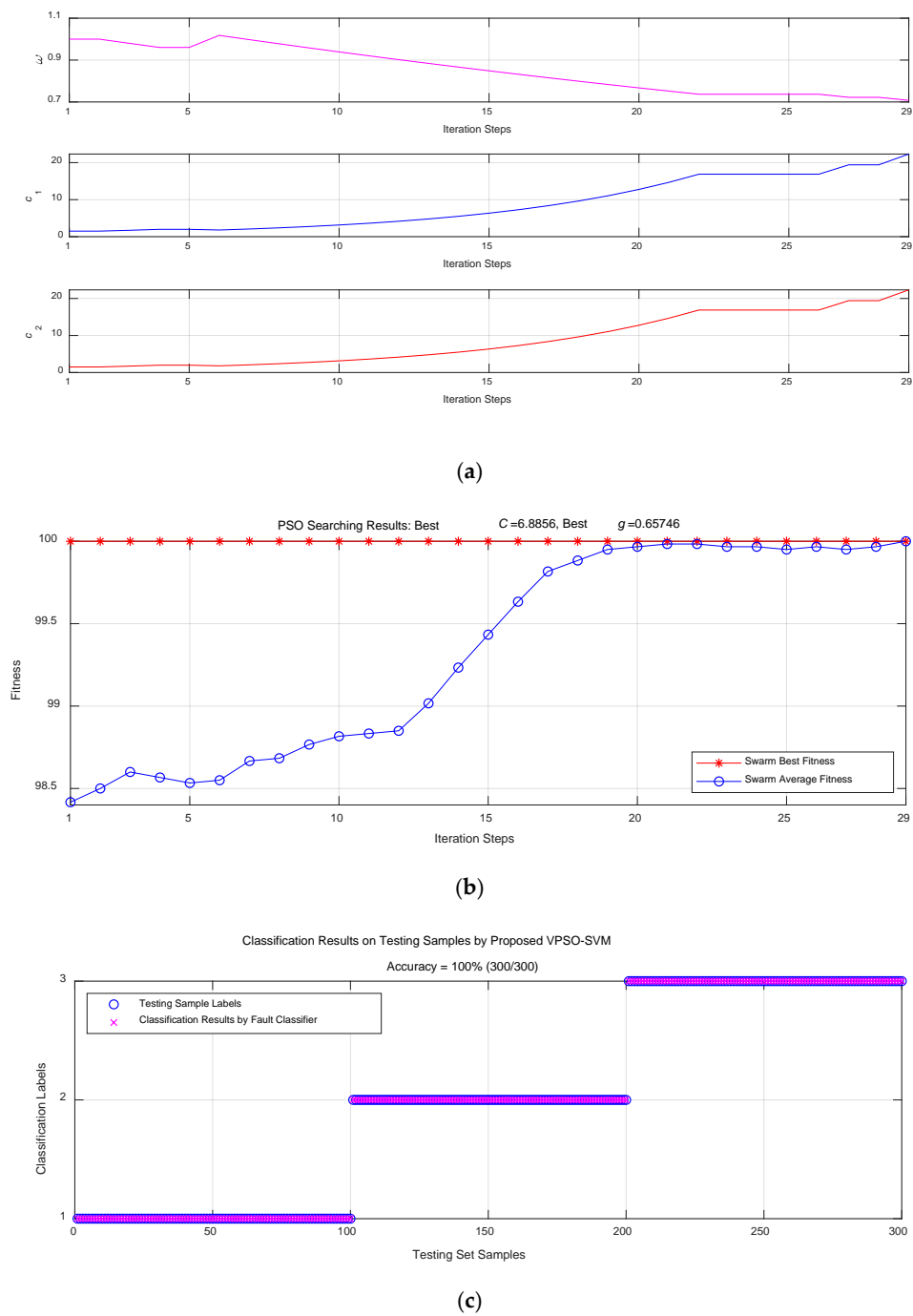


Figure 14. Fault classification results on testing set by VPSO-SVM with SVM parameters $C = 6.8856$ and $g = 0.65746$ optimized by CPSO. (a) Variation curves of c_1 , c_2 and ω in PSO along with iterations. (b) Swarm average fitness evolving process along iterations (29 iteration steps to converge with variable c_1 , c_2 and ω in PSO). (c) Fault classification results of VPSO-SVM with classification accuracy = 100%.

Table 4. Simulation results statistical data of the three comparative methods.

	SVM	CPSO-SVM	VPSO-SVM
Elapsed Time on Training (s)	0.001976	18.527162	8.469169
Classification Accuracy on Testing Set Samples (correctly classified samples/total samples)	99.33% (298/300)	100% (300/300)	100% (300/300)
PSO Iteration Steps	-	73	29

From Figure 12 and Table 4, it could be seen that if only SVM (with manually assigned parameters values) was adopted for fault classification, the training of SVM is very fast and only took less than 0.002 s. But the assigned SVM parameters were not optimized, this meant 2 samples among 300 testing ones were improperly classified, and the classification accuracy was 99.33%.

When the parameters of SVM were optimized by CPSO, it can be seen from Figure 13b and Table 4 that the SVM classification accuracy increased to 100%, 300 samples of testing set were correctly classified. However, searching optimal SVM parameter values took time; the CPSO with constant c_1 , c_2 and ω values iterated 73 generations to find the optimal values of $C = 6.8856$ and $g = 0.65746$, as shown in Figure 13a, and the total PSO iteration and SVM training time was 18.53 s.

When the proposed VPSO method was adopted for optimal SVM parameter searching, the variation of c_1 , c_2 and ω of PSO along with iterations (shown in Figure 14a) helped the PSO decrease its iteration steps from 73 to 29 before it could find the same optimal values of $C = 6.8856$ and $g = 0.65746$ (shown in Figure 14b and Table 4). The variable parameter mechanism of VPSO accelerated the convergent speed, and the total PSO iteration and SVM training time decreased from 18.53 to 8.47 s. With the same optimal parameter values, the SVM achieved the same classification accuracy of 100% (shown in Figure 14c and Table 4).

With this trained VPSO-SVM, in case OCFs are detected by the OCF indicator, the diagnosis of the three types of fault could be realized by inputting the exacted features of FP-PMGS terminal currents and outputting its predicted fault label, which indicates the fault type.

4.4. Faulty Phase Diagnosis Simulations of Single-Phase OCFs and Results Comparison

In Section 4.3, the VPSO-SVM is applied to diagnose the three different OCFs. In this section, the proposed method is used to identify which phase is suffering an OCF when single-phase OCF is happening in the FP-PMSG.

Ran the simulation platform shown in Figure 2 five times, the simulation durations were all 0.3 s. The single-phase OCF simulation procedures are as follows:

- (1) in the 1st simulation, from 0 to 0.1 s and from 0.2 to 0.3 s, the MCGS was running normally, while from 0.1 to 0.2 s, a single-phase OCF happened in phase a ;
- (2) in the 2nd simulation, from 0 to 0.1 s and from 0.2 to 0.3 s, the MCGS was running normally, while from 0.1 to 0.2 s, a single-phase OCF happened in phase b ;
- (3) in the 3rd simulation, from 0 to 0.1 s and from 0.2 to 0.3 s, the MCGS was running normally, while from 0.1 to 0.2 s, a single-phase OCF happened in phase c ;
- (4) in the 4th simulation, from 0 to 0.1 s and from 0.2 to 0.3 s, the MCGS was running normally, while from 0.1 to 0.2 s, a single-phase OCF happened in phase d ;
- (5) in the 5th simulation, from 0 to 0.1 s and from 0.2 to 0.3 s, the MCGS was running normally, while from 0.1 to 0.2 s, a single-phase OCF happened in phase e .

We collected the five-phase output currents of the FP-PMSG in each simulation and applied frame transformation to obtain the direct-axis components of the five simulations. The direct-axis currents in the five simulations are shown in Figure 15. We applied EMD to those i_{d1} shown in Figure 15 to obtain IMFs and residues, which are shown in Figure 16.

From Figure 15, it could be seen that the single-phase OCF in different FP-PMSG phases leads to disturbances in the direct-axis current components: the OCFs in phases a , c and d cause distinct variations to i_{d1} with different patterns, while OCFs in phases b and e made i_{d1} slightly change. However, all the variation patterns on i_{d1} are different from each other, which could contribute to the faulty phase diagnosis.

It could be seen from Figure 16, the EMD extracted four IMFs and one residue from i_{d1} when the OCF happened in phase a , c , d and e , but only three IMFs when the OCF happened in phase b . To make features of five single-phase OCF have the same dimensions, 0 s were filled in data array as the non-existent IMF4 when the OCF happened in phase b . Accordingly, after Hilbert transform to the

four IMFs and one residue of the five faulty signals, and after calculating the instantaneous amplitude, phase and frequency, a 1-by-15 feature vector is obtained for each sampled current data.

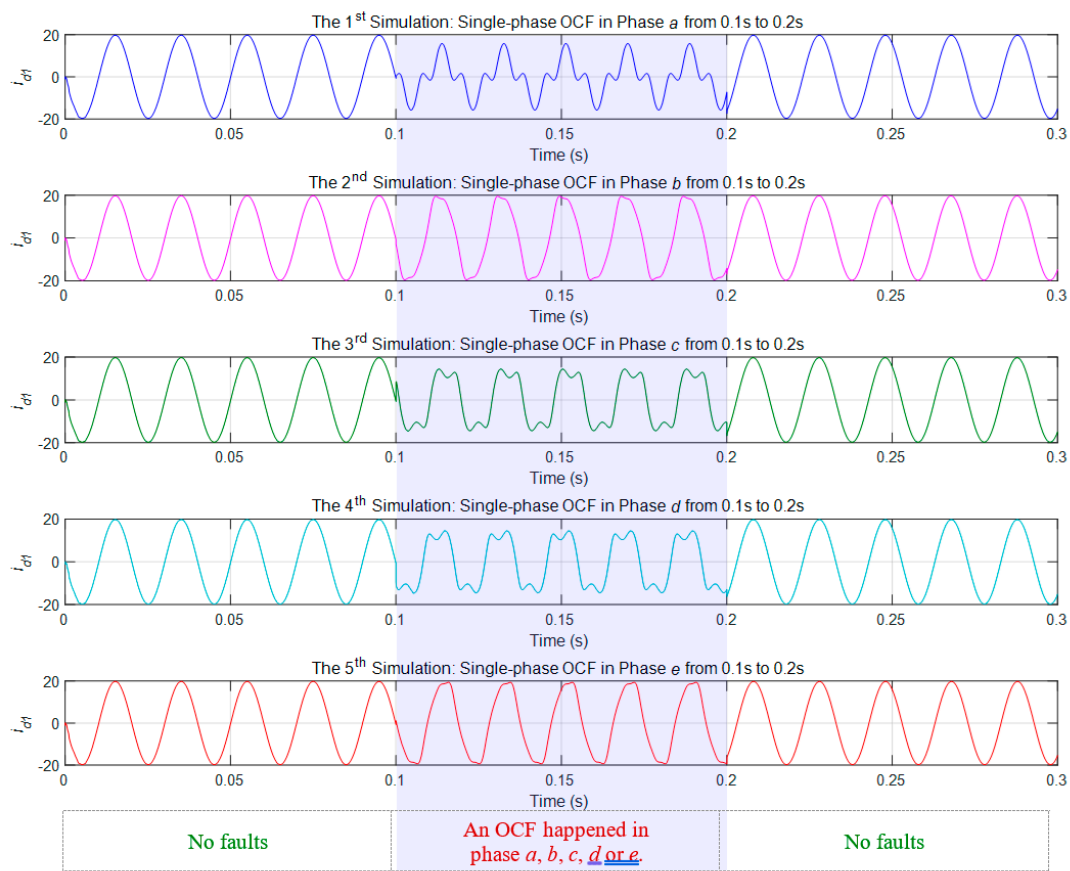


Figure 15. Direct-axis components of five-phase fundamental currents in five simulations with single-phase OCF occurring in each phase of the FP-PMSG.

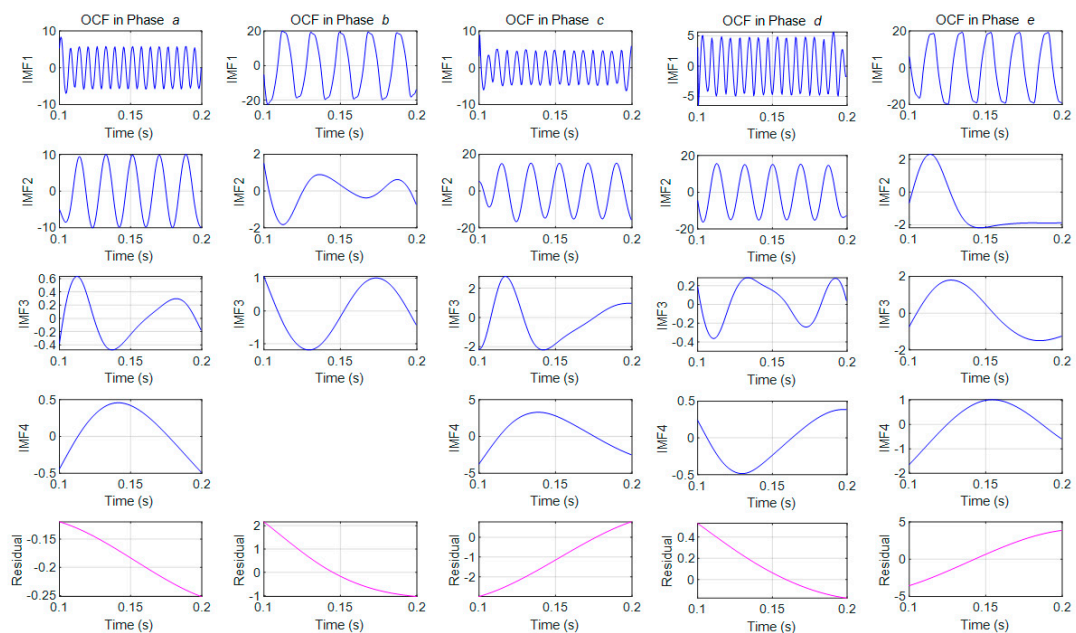


Figure 16. IMFs and residue of direct-axis current in five simulations.

In total 1000 samples were extracted from the five single-phase OCF simulations, 200 in each from 0.1 to 0.2 s when there was an OCF. All samples were evenly distributed over time. Here, a 1000-by-15 feature matrix was obtained. Classification labels were assigned to the five single-phase OCFs as follows:

- Label "1" is for single-phase OCF in phase *a*,
- Label "2" is for single-phase OCF in phase *b*,
- Label "3" is for single-phase OCF in phase *c*,
- Label "4" is for single-phase OCF in phase *d*,
- Label "5" is for single-phase OCF in phase *e*.

The collected samples and their labels are shown in Figure 17.

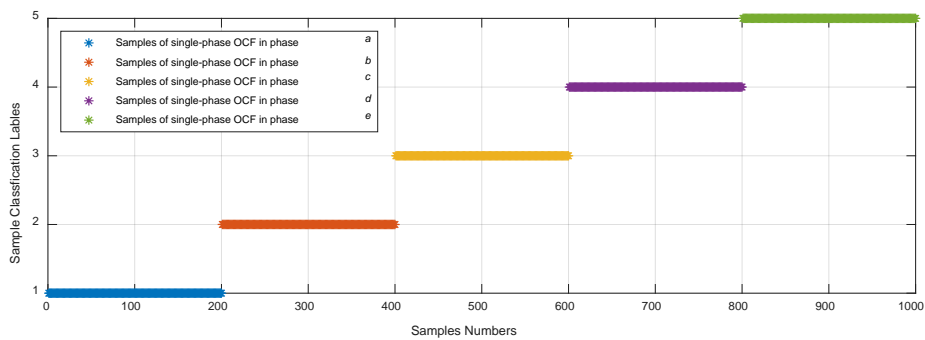


Figure 17. The 1000 samples with their corresponding labels.

Among the 200 samples of each single-phase OCF, 100 were taken to train an SVM and the remaining 100 were used to test the trained SVM. Thus, the training and testing sets both had 500 samples for the five faults. These samples were loaded to the VPSO-SVM method. To compare the effectiveness of the proposed VPSO-SVM, the fault features were also applied to an SVM with constant *C* and *g*, and the CPSO-SVM with invariant parameters of PSO. These three contrastive methods had the same parameter settings as used in the last section. To remove the disturbances from randomly generated values in PSO on the classification results, the same initial values as used in the last section were assigned to the swarm particles.

The fault classification results on the testing set by SVM with fixed parameters *C* and *g* are shown in Figure 18. The PSO iteration process and fault classification results on the testing set by CPSO-SVM are shown in Figure 19. The PSO parameter variation plots along with iterations, PSO iteration process, and fault classification results on the testing set by the proposed VPSO-SVM are shown in Figure 20. The simulation results' statistical data of the three comparative methods are summarized in Table 5.

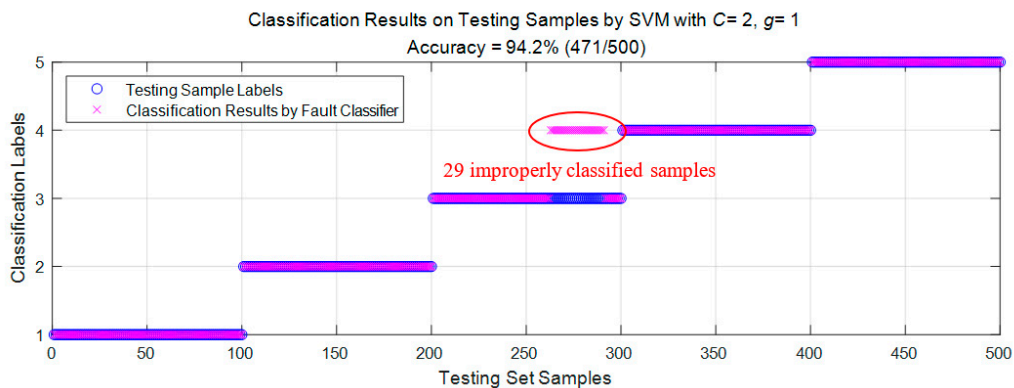
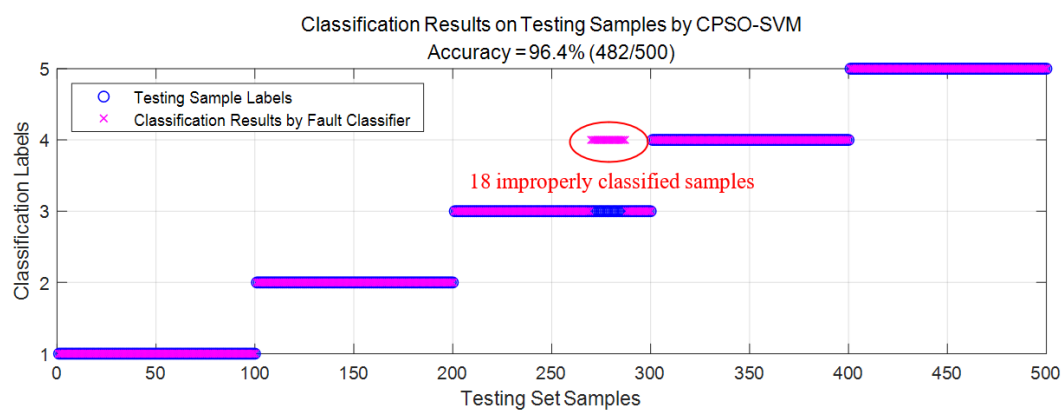


Figure 18. Fault classification results on testing set by SVM with assigned parameters *C* = 2 and *g* = 1 (classification accuracy = 94.2%).



(a)



(b)

Figure 19. Fault classification results on testing set by CPSO-SVM with SVM parameters $C = 10$ and $g = 0.01$ optimized by CPSO. (a) Swarm average fitness evolving process along with iterations (88 iteration steps to converge with constant $c_1 = c_2 = 1.5$ and $\omega = 1$ in PSO). (b) Fault classification results of CPSO-SVM (classification accuracy = 96.4%).

Table 5. Simulation results statistical data of the three comparative methods.

	SVM	CPSO-SVM	VPSO-SVM
Elapsed Time on Training (s)	0.004017	83.073914	33.393072
Classification Accuracy on Testing Samples (correctly classified samples/total samples)	94.2% (471/500)	96.4% (482/500)	96.4% (482/500)
PSO Iteration Steps	-	88	33

From Figure 18 and Table 5, it could be seen that if only SVM (with manually assigned parameters $C = 2$ and $g = 1$) was adopted for fault classification, the training time of SVM is only 0.004 s. But the assigned SVM parameters were not optimized, this made the classification accuracy 94.2%, and 29 samples among 500 were improperly classified.

When the parameters of SVM were optimized by CPSO, it can be seen from Figure 19b and Table 5 that the SVM classification accuracy increased from 94.2% to 96.4%, and wrongly classified sample numbers decreased to from 29 to 18. However, searching optimal SVM parameters took time, the CPSO with constant c_1 , c_2 and ω values iterated 88 generations to find the optimal values of $C = 10$ and $g = 0.01$, and as shown in Figure 19a, the total PSO iteration and SVM training time was 83.07 s.

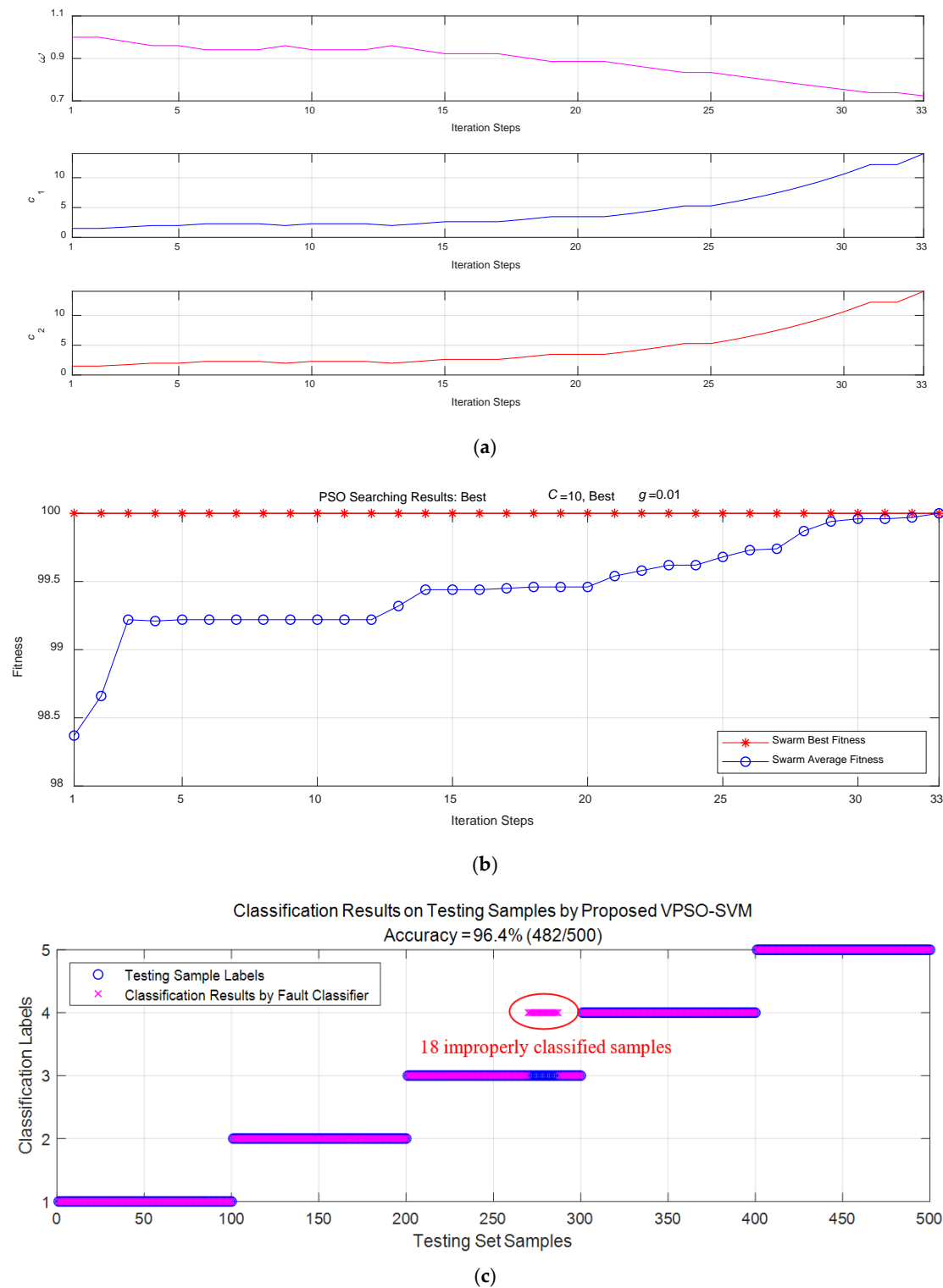


Figure 20. Fault classification results on testing set by VPSO-SVM with SVM parameters $C = 10$ and $g = 0.01$ optimized by CPSO. (a) Variation curves of c_1 , c_2 and ω in PSO along with iterations. (b) Swarm average fitness evolving process along iterations (33 iteration steps to converge with variable c_1 , c_2 and ω in PSO). (c) Fault classification results of VPSO-SVM with classification accuracy = 96.4%.

When the proposed VPSO method was applied for optimal SVM parameter searching, the variation of c_1 , c_2 and ω of PSO along with iterations (shown in Figure 20a) helped the PSO decrease its iteration

steps from 88 to 33 before it could find the same optimal values of $C = 10$ and $g = 0.01$ (shown in Figure 20b and Table 5). The variable parameter mechanism of VPSO accelerated the convergent speed, and the total PSO iteration and SVM training time decreased from 83.07 s to 33.39 s. With the same optimal parameter values, the SVM achieved the same classification accuracy of 96.4% (as shown in Figure 20c and Table 5).

With the trained VPSO-SVM in this section, in case single-phase OCF is detected by the fault indicator, faulty phase could be diagnosed by inputting the exacted features of FP-PMGS terminal currents and outputting the predicted label, which indicates which phase is suffering a single-phase OCF with a high prediction accuracy.

5. Conclusions and Discussion

This article focuses on fault detection and diagnosis techniques of a non-salient FP-PMMSG with THWs for marine tidal generation applications. The main FP-PMMSG faults considered in this paper include three types: (1) single-phase OCF, (2) simultaneous OCFs in two adjacent phases, and (3) simultaneous OCFs in two non-adjacent phases. The researched FDD techniques are based on EMD, Hilbert transform, PSO and SVM methods.

To realize fault detection of OCFs in FP-PMMSG, EMD and Hilbert transform are applied on the direct-axis components of the FP-PMMSG terminal currents. The instantaneous amplitude of the complex analytic single after Hilbert transform applied on the first IMF is selected as the OCF indicator to show the occurrence time of the faults.

Then, a fault classifier based on VPSO-SVM is proposed to diagnose the faults. In this composite method, SVM is the main classifier for fault type identification, and PSO is adopted to search optimal values of penalty coefficient C and kernel parameter g , which are very important for the classification accuracy of SVM. In order to accelerate the convergence speed of PSO with cross-validations, a swarm average fitness-based parameter variation mechanism is designed to tune the cognitive- and social-learning rates and the inertia weight of PSO along with the iteration process.

To validate the effectiveness of the proposed method, the models of MCGS based on a FP-PMMSG with THWs was built and realized with MATLAB/Simulink. Simulation results and comparisons showed that the proposed VPSO-SVM could offer higher fault classification accuracy than SVM with manually assigned parameters and faster convergence speed than CPSO-SVM. The method could not only diagnosis the three different OCFs in FP-PMMSG, but also identify the faulty phase with high accuracy when a single-phase OCF happens.

What should be mentioned here is that the initial values of the swarm particles were very important to decide the convergence speed of PSO. During the simulations, although it did not often happen, some 'lucky' initial values of particles made the optimal values searching process very fast. In such cases, there was no need to apply the proposed swarm average fitness-based parameter variation mechanism to PSO. However, in most cases, this mechanism could help. So, in this paper, same initial values generated with the MATLAB *rand* function were assigned to the particles in all simulations to avoid disturbance of the convergence time by random initial values.

It should be realized that FDD of multi-phase MCGSs are complex problems, and faults are more diverse and complex than those of traditional three-phase generation systems. For example, electrical faults can arise in various phases of both generators and converters; measured signals for FDD may contain noises caused by MCGSs' time-varying operation conditions; turbine blades with attached underwater organisms could introduce harmonics in generators. All these complexities make FDD research of MCGSs very interesting and full of challenges. Accordingly, subsequent research of this paper will deal with several important issues that have not been solved in this paper, such as FDD of MCGSs' five-phase converters, hybrid faults diagnosis of generators, FDD of concurrent faults in both generators and converters, and incipient fault diagnosis and prediction of MCGSs. Furthermore, more practical considerations, such as the impact of tidal speed and load variations, disturbance from

ocean environments, dynamic behavior ignorance in the research processes, etc. will be gradually taken into account to make the research results more realistic.

Author Contributions: Conceptualization, G.Y.; software, S.P. and T.Y.; methodology, M.B.; validation, M.A.-A. and M.F.B. All authors have read and agreed to the published version of the manuscript.

Funding: This research was funded by the Shanghai Science and Technology Committee Foundation with Grant No. 19040501700, the Zhejiang Provincial Natural Science Foundation of China with Grant No. LR17F030005, and the National Natural Science Foundation of China with Grant No. 61673260.

Conflicts of Interest: The authors declare no conflict of interest.

References

- Djebbari, S.; Charpentier, J.F.; Scullier, F.; Benbouzid, M. Design and Performance Analysis of Double Stator Axial Flux PM Generator for Rim Driven Marine Current Turbines. *IEEE J. Ocean. Eng.* **2016**, *41*, 50–66. [[CrossRef](#)]
- Elghali, S.E.B.; Balme, R.; Le Saux, K.; Benbouzid, M.E.H.; Charpentier, J.F.; Hauville, F. A Simulation Model for the Evaluation of the Electrical Power Potential Harnessed by a Marine Current Turbine. *IEEE J. Ocean. Eng.* **2007**, *32*, 786–797. [[CrossRef](#)]
- Khan, M.J.; Iqbal, M.T.; Quaicoe, J.E. Dynamics of a vertical axis hydrokinetic energy conversion system with a rectifier coupled multi-pole permanent magnet generator. *IET Renew. Power Gener.* **2010**, *4*, 116–127. [[CrossRef](#)]
- Gong, B.; Wang, K.; You, J.; Meng, F.; Luo, Y. A novel phase-locked loop for power converters of ocean current power generation system. In Proceedings of the 2014 IEEE International Conference on Mechatronics and Automation, Tianjin, China, 3–6 August 2014; pp. 1984–1989. [[CrossRef](#)]
- Fall, O.; Charpentier, J.F.; Nguyen, N.K.; Letellier, P. Performances comparison of different concentrated-winding configurations for 5-phase PMSG in normal and faulty modes in flux weakening operation for fixed pitch tidal turbines. In Proceedings of the 2016 XXII International Conference on Electrical Machines (ICEM), Lausanne, Switzerland, 13–14 June 2016; pp. 2789–2795. [[CrossRef](#)]
- Fall, O.; Charpentier, J.F.; Nguyen, N.K.; Letellier, P. Maximum torque per ampere control strategy of a 5-phase PM generator in healthy and faulty modes for tidal marine turbine application. In Proceedings of the 2014 International Power Electronics and Application Conference and Exposition, Shanghai, China, 5–8 November 2014; pp. 468–473. [[CrossRef](#)]
- Li, G.J.; Ren, B.; Zhu, Z.Q. Design guidelines for fractional slot multi-phase modular permanent magnet machines. *IET Electr. Power Appl.* **2017**, *11*, 1023–1031. [[CrossRef](#)]
- Abd Hafez, A.A.; Todd, R.; Forsyth, A.J.; Cross, A.M. Direct current ripple compensation for multi-phase fault-tolerant machines. *IET Electr. Power Appl.* **2011**, *5*, 28–36. [[CrossRef](#)]
- Zoric, I.; Jones, M.; Levi, E. Arbitrary d–q current sharing in three-phase winding sets of multi-phase machines. *J. Eng.* **2019**, *2019*, 4173–4177. [[CrossRef](#)]
- Dwari, S.; Parsa, L. Fault-Tolerant Control of Five-Phase Permanent-Magnet Motors with Trapezoidal Back EMF. *IEEE Trans. Ind. Electron.* **2011**, *58*, 476–485. [[CrossRef](#)]
- Wang, K.; Gu, Z.Y.; Liu, C.; Zhu, Z.Q. Design and Analysis of a Five-Phase SPM Machine Considering Third Harmonic Current Injection. *IEEE Trans. Energy Convers.* **2018**, *33*, 1108–1117. [[CrossRef](#)]
- Cruz, S.M.; Ferreira, M.; Mendes, A.M.; Cardoso, A.J.M. Analysis and Diagnosis of Open-Circuit Faults in Matrix Converters. *IEEE Trans. Ind. Electron.* **2011**, *58*, 1648–1661. [[CrossRef](#)]
- Ferdjallah-Kherkhachi, E.; Schaeffer, E.; Loron, L.; Benbouzid, M.E.H. Online monitoring of marine turbine insulation condition based on high frequency models: Methodology for finding the “best” identification protocol. In Proceedings of the IECON 2014—40th Annual Conference of the IEEE Industrial Electronics Society, Dallas, TX, USA, 29 October–1 November 2014; pp. 3374–3380. [[CrossRef](#)]
- Benelghali, S.; Benbouzid, M.E.H.; Charpentier, J.F. Generator Systems for Marine Current Turbine Applications: A Comparative Study. *IEEE J. Ocean. Eng.* **2012**, *37*, 554–563. [[CrossRef](#)]
- Wang, L.; Lin, Y.; Lo, T. Implementation and Measurements of a Prototype Marine-Current Power Generation System on Peng-Hu Island. *IEEE Trans. Ind. Appl.* **2015**, *51*, 651–657. [[CrossRef](#)]

16. Arzu, F.; Darvishi, H.H.; Hashim, R.B.; Ghazvinei, P.T.; Soeb, M.R. Numerical investigation on the hydrodynamic performance of variable length blade tidal turbine: An attribute to enhance energy capture. *IET Renew. Power Gener.* **2017**, *11*, 347–352. [[CrossRef](#)]
17. Vybulkova, L.; Vezza, M.; Brown, R. Simulating the Wake Downstream of a Horizontal Axis Tidal Turbine Using a Modified Vorticity Transport Model. *IEEE J. Ocean. Eng.* **2016**, *41*, 296–301. [[CrossRef](#)]
18. Pham, H.T.; Bourgeot, J.M.; Benbouzid, M.E.H. Comparative Investigations of Sensor Fault-Tolerant Control Strategies Performance for Marine Current Turbine Applications. *IEEE J. Ocean. Eng.* **2018**, *43*, 1024–1036. [[CrossRef](#)]
19. Elghali, S.E.B.; Benbouzid, M.E.H.; Ahmed-Ali, T.; Charpentier, J.F. High-Order Sliding Mode Control of a Marine Current Turbine Driven Doubly-Fed Induction Generator. *IEEE J. Ocean. Eng.* **2010**, *35*, 402–411. [[CrossRef](#)]
20. Benelghali, S.; Benbouzid, M.E.H.; Charpentier, J.F.; Ahmed-Ali, T.; Munteanu, I. Experimental Validation of a Marine Current Turbine Simulator: Application to a permanent magnet synchronous generator-based system second-order sliding mode control. *IEEE Trans. Ind. Electron.* **2011**, *58*, 118–126. [[CrossRef](#)]
21. Chen, H.; At-Ahmed, N.; Machmoum, M.; Zam, M.E.H. Modeling and Vector Control of Marine Current Energy Conversion System Based on Doubly Salient Permanent Magnet Generator. *IEEE Trans. Sustain. Energy* **2016**, *7*, 409–418. [[CrossRef](#)]
22. Wang, L.; Liu, J.H. Dynamic Analysis of a Grid-Connected Marine-Current Power Generation System Connected to a Distribution System. *IEEE Trans. Power Syst.* **2010**, *25*, 1798–1805. [[CrossRef](#)]
23. Mekri, F.; Elghali, S.B.; Benbouzid, M.E.H. Fault-Tolerant Control Performance Comparison of Three- and Five-Phase PMSG for Marine Current Turbine Applications. *IEEE Trans. Sustain. Energy* **2013**, *4*, 425–433. [[CrossRef](#)]
24. Zhou, Z.; Scuiller, F.; Charpentier, J.F.; Benbouzid, M.E.H.; Tang, T. Power Control of a Nonpitchable PMSG-Based Marine Current Turbine at Overrated Current Speed with Flux-Weakening Strategy. *IEEE J. Ocean. Eng.* **2015**, *40*, 536–545. [[CrossRef](#)]
25. Zhang, M.; Wang, T.; Tang, T. A multi-mode process monitoring method based on mode-correlation PCA for Marine Current Turbine. In Proceedings of the 2017 IEEE 11th International Symposium on Diagnostics for Electrical Machines, Power Electronics and Drives (SDEMPED), Tinos, Greece, 29 August–1 September 2017; pp. 286–291. [[CrossRef](#)]
26. Ferdjallah-Kherkhachi, E.; Schaeffer, E.; Loron, L.; Benbouzid, M.E.H. Effect of the short-term temperature changes on Diagnostic Indicator in online insulation monitoring by parametric identification. In Proceedings of the 2015 IEEE 24th International Symposium on Industrial Electronics (ISIE), Buzios, Brazil, 3–5 June 2015; pp. 822–826. [[CrossRef](#)]
27. Zhang, M.; Wang, T.; Tang, T.; Benbouzid, M.; Diallo, D. Imbalance fault detection of marine current turbine under condition of wave and turbulence. In Proceedings of the IECON 2016—42nd Annual Conference of the IEEE Industrial Electronics Society, Florence, Italy, 23–26 October 2016; pp. 6353–6358. [[CrossRef](#)]
28. Choqueuse, V.; Benbouzid, M.E.H. Non-stationary spectral estimation for wind turbine induction generator faults detection. In Proceedings of the IECON 2013—39th Annual Conference of the IEEE Industrial Electronics Society, Vienna, Austria, 10–13 November 2013; pp. 7376–7381. [[CrossRef](#)]
29. Arafat, A.K.M.; Choi, S.; Baek, J. Open-Phase Fault Detection of a Five-Phase Permanent Magnet Assisted Synchronous Reluctance Motor Based on Symmetrical Components Theory. *IEEE Trans. Ind. Electron.* **2017**, *64*, 6465–6474. [[CrossRef](#)]
30. Immovilli, F.; Bianchini, C.; Lorenzani, E.; Bellini, A.; Fornasiero, E. Evaluation of Combined Reference Frame Transformation for Interturn Fault Detection in Permanent-Magnet Multiphase Machines. *IEEE Trans. Ind. Electron.* **2015**, *62*, 1912–1920. [[CrossRef](#)]
31. Hu, R.; Wang, J.; Sen, B.; Mills, A.R.; Chong, E.; Sun, Z. PWM Ripple Currents Based Turn Fault Detection for Multiphase Permanent Magnet Machines. *IEEE Trans. Ind. Appl.* **2017**, *53*, 2740–2751. [[CrossRef](#)]
32. Sen, B.; Wang, J. Stator Interturn Fault Detection in Permanent-Magnet Machines Using PWM Ripple Current Measurement. *IEEE Trans. Ind. Electron.* **2016**, *63*, 3148–3157. [[CrossRef](#)]
33. Sundaram, V.M.; Toliyat, H.A. Stator inter-turn fault detection for seamless fault-tolerant operation of five-phase induction motors. In Proceedings of the 2016 IEEE Energy Conversion Congress and Exposition (ECCE), Milwaukee, WI, USA, 18–22 September 2016; pp. 1–8. [[CrossRef](#)]

34. Salehifar, M.; Arashloo, R.S.; Moreno-Equilaz, J.M.; Sala, V.; Romeral, L. Fault Detection and Fault Tolerant Operation of a Five Phase PM Motor Drive Using Adaptive Model Identification Approach. *IEEE J. Emerg. Sel. Top. Power Electron.* **2014**, *2*, 212–223. [[CrossRef](#)]
35. Perveen, R.; Kishor, N.; Mohanty, S.R. Fault detection for offshore wind farm connected to onshore grid via voltage source converter-high voltage direct current. *IET Gener. Transm. Distrib.* **2015**, *9*, 2544–2554. [[CrossRef](#)]
36. Yue, M.; Ait-Ahmed, M.; Benkhoris, M.F.; Yao, G. A HHT based fault detection method of a multiphase generator—Diode rectifier se. In Proceedings of the IECON 2017—43rd Annual Conference of the IEEE Industrial Electronics Society, Beijing, China, 5–8 November 2017; pp. 8311–8316. [[CrossRef](#)]
37. Xie, L.; Tang, T. Modeling and control of a small marine current power generation system. In Proceedings of the 2012 IEEE International Symposium on Industrial Electronics, Hangzhou, China, 18–20 October 2012; pp. 1438–1443. [[CrossRef](#)]
38. Yao, N.; Zhang, F.; Cai, Z.; Rao, K.; Xu, M. The effect of moment of inertia on the transformation efficiency of a turbine for underwater motors. In Proceedings of the 2017 4th International Conference on Systems and Informatics (ICSAI), Hangzhou, China, 11–13 November 2017; pp. 412–417. [[CrossRef](#)]
39. Mousa, H.H.; Youssef, A.R.; Mohamed, E.E. Optimal power extraction control schemes for five-phase PMSG based wind generation systems. *Eng. Sci. Technol. Int. J.* **2020**, *23*, 144–155. [[CrossRef](#)]
40. Yuan, J.; Jiang, H.; Zhao, Q.; Xu, C.; Liu, H.; Tian, Y. Dual-Mode Noise-Reconstructed EMD for Weak Feature Extraction and Fault Diagnosis of Rotating Machinery. *IEEE Access* **2019**, *7*, 173541–173548. [[CrossRef](#)]
41. Alvarez-Gonzalez, F.; Griffio, A.; Wang, B. Permanent magnet synchronous machine stator windings fault detection by Hilbert–Huang transform. *J. Eng.* **2019**, *2019*, 3505–3509. [[CrossRef](#)]
42. Chen, G.; Cai, X. Reconfigurable Control for Fault-Tolerant of Parallel Converters in PMSG Wind Energy Conversion System. *IEEE Trans. Sustain. Energy* **2019**, *10*, 604–614. [[CrossRef](#)]
43. Zidi, S.; Moulahi, T.; Alaya, B. Fault Detection in Wireless Sensor Networks Through SVM Classifier. *IEEE Sens. J.* **2018**, *18*, 340–347. [[CrossRef](#)]
44. Jan, S.U.; Lee, Y.; Shin, J.; Koo, I. Sensor Fault Classification Based on Support Vector Machine and Statistical Time-Domain Features. *IEEE Access* **2017**, *5*, 8682–8690. [[CrossRef](#)]
45. Wang, Y.; Wang, D.; Tang, Y. Clustered Hybrid Wind Power Prediction Model Based on ARMA, PSO-SVM, and Clustering Methods. *IEEE Access* **2020**, *8*, 17071–17079. [[CrossRef](#)]
46. Divyajot; Kumar, R.; Fozdar, M. Optimal sizing of hybrid ship power system using variants of particle swarm optimization. In Proceedings of the 2017 International Conference on Recent Developments in Control, Automation & Power Engineering (RDCAPE), Noida, India, 26–27 October 2017; pp. 527–532. [[CrossRef](#)]
47. Ding, S.; Hang, J.; Wei, B.; Wang, Q. Modelling of supercapacitors based on SVM and PSO algorithms. *IET Electr. Power Appl.* **2018**, *12*, 502–507. [[CrossRef](#)]

Publisher’s Note: MDPI stays neutral with regard to jurisdictional claims in published maps and institutional affiliations.



© 2020 by the authors. Licensee MDPI, Basel, Switzerland. This article is an open access article distributed under the terms and conditions of the Creative Commons Attribution (CC BY) license (<http://creativecommons.org/licenses/by/4.0/>).